Chapter 2
Channel Measurements

Chapter Editor Nicolai Czink, Alexis Paolo Garcia Ariza, Katsuyuki Haneda, Martin Jacob, Johan Kåredal, Martin Käske, Jonas Medbo, Juho Poutanen, Jussi Salmi, Gerhard Steinböck, and Klaus Witrisal

Radio channel measurements and channel modeling have always been a driving force of the wireless COST actions. These high spirits have been kept up also in COST 2100, where significant advances, particularly in channel measurements, have been made.

Channel measurements are indispensable for wireless system design. It is the wireless channel that determines the ultimate performance limits of any communication system. In the beginnings of cellular communications, fading and path loss of the narrowband channel were the key figures of merit. This has changed with wideband multiantenna, multiuser systems. New important features of the radio channel became obvious: the channels' frequency selectivity, directivity, polarimetric properties, and their relation to channels of the other users.

Also for emerging systems, the channel properties need to be identified and modeled: Peer-to-peer systems, which employ distributed nodes indoors or outdoors, show surprising fading characteristics. The propagation channels between vehicles suffer from severe fading under high Doppler shifts. Ultrawideband systems provide an extremely high delay resolution, which needs to be captured. Finally, radio systems using millimeter and submillimeter waves experience strong shadowing by human bodies. All these effects need to be measured and modeled accordingly.

Once measurements have been done, and researchers obtained an abundance of data, these measurements need to be analyzed in a sound way. For modeling purposes it is often advantageous to separate the effects of the antenna from the radio channel. This can be achieved by high-resolution parameter estimation, where the channel is characterized as a superposition of multiple wave fronts. Using this data along with maps or photographs of the environment, scattering objects can be automatically located, which provides a deep insight into the processes going on in the radio channel. However, high-resolution parameter estimation methods have several pitfalls, depending on the calibration of the measurement equipment. Only with the knowledge of possible pitfalls, these can be avoided.

N. Czink (✉)
Forschungszentrum Telekommunikation Wien (FTW), Vienna, Austria

R. Verdone, A. Zanella (eds.), *Pervasive Mobile and Ambient Wireless Communications*, Signals and Communication Technology,
DOI 10.1007/978-1-4471-2315-6_2,

Due to the large number of successful measurement campaigns in all these areas, and the consequential results, it is impossible to describe all the findings in depth. This chapter rather presents a summary of the measurements methods including respective examples and provides references for further reading.

The first part of this chapter gives an overview of recent advances in channel measurements in Sect. 2.1. Starting with measuring distributed, cooperative communication systems in Sect. 2.1.1, the discussion continues with the specificities of polarimetric channel measurements in Sect. 2.1.2. Next, the challenges of measuring channels with high mobility are described in Sect. 2.1.3. Subsequently, the methods of ultrawideband channel sounding are shortly outlined in Sect. 2.1.4. Finally, the measurements and channel characteristics of millimeter and submillimeter channels are discussed in depth in Sect. 2.1.5.

The second part of this chapter in Sect. 2.2 is devoted to recent methods of measurement analysis. First, different approaches for high-resolution parameter estimation are discussed in Sect. 2.2.1. Subsequently, Sect. 2.2.2 describes how to localize and visualize scattering in the environment. Finally, the pitfalls of high-resolution parameter estimation are pointed out in Sect. 2.2.3. Finally, Sect. 2.3 draws the conclusions from this chapter by walking through the lessons learned.

The evaluation of the measurement data and consecutive radio channel modeling is not part of this chapter. These aspects are addressed in the following chapters, specific to the considered systems.

2.1 Advances in Channel Measurements

This section discusses the latest methods to measure the radio channels of different kinds of systems. Due to the broad nature of the research in recent years, a number of different topics is addressed: Distributed cooperative systems, the polarimetric channel, vehicular channels under high mobilities, ultrawideband channel sounding, and millimeter and submillimeter wave systems.

2.1.1 Measuring Distributed Systems

We use the term "distributed systems" for the whole range from distributed ad hoc networks to cooperating base stations in a cellular system. All these systems have in common that they are typically wideband, make use of multiple antennas at each node and suffer from interference. These properties need to be measured and modeled accordingly. In this section, we focus on the different ways to measure distributed systems.

Generally, the techniques for measuring distributed systems can broadly be split into three methods:

Single-sounder sequential measurements In these measurements, a single-channel sounder equipment is used sequentially along multiple routes to mimic multiple

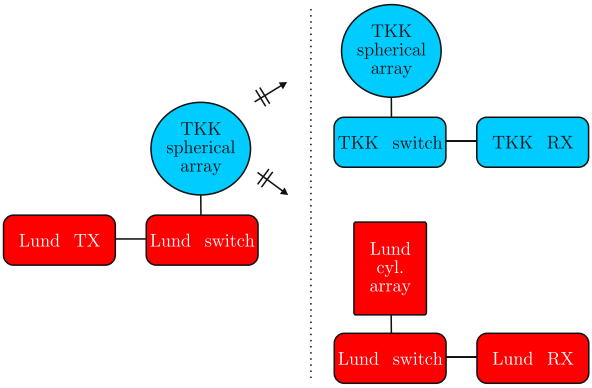

Fig. 2.1 Setup of the WILATI indoor multiuser MIMO measurements [KAS+] (©2010 IEEE, reproduced with permission)

users in a sufficiently static scenario. Another possibility is to measure the same route sequentially with different base station positions. For this reason, this kind of measurement is sometimes also called "multipass measurements."

Single-sounder multinode measurements Again, only a single-channel sounder is used, however multiple nodes are connected to the sounder by long RF cables. In this way, the nodes can be distributed across multiple rooms in a building (or even farther when using optical RF cables).

Multi-sounder measurements This type of measurements employs multiple channel sounders, where typically a single transmitter and multiple receivers are used.

Since there are multiple ways to implement these three methods, this section will provide an overview of recent measurement activities in *different scenarios* explaining the key ideas, the measurement method, and an exemplary result. The following paragraphs are organizing the scenarios into *multinode* (multiuser) measurements and *multibase-station* measurements.

2.1.1.1 Multinode Measurements

Multinode measurements comprise both measurements with a single base station and multiple users, and also peer-to-peer measurements.

Indoor Multiuser MIMO With huge technological effort, Aalto University and Lund University (LU) married their fundamentally different channel sounders to do multiuser Multiple-Input Multiple-Output (MIMO) measurements [KAS+, RTR+08] in the WILATI project. The general system setup is shown in Fig. 2.1.

The LU sounder is a commercial RUSK channel sounder produced by MEDAV GmbH [cha10]. It uses fast Radio Frequency (RF) switching and periodic multifrequency signals. The transmitter of the LU sounder has an arbitrary waveform generator unit. The receiver equipment is down converting, sampling, and processing the signal.

Table 2.1 Lund University and Aalto University sounder specifications

Parameter	LU sounder	Aalto sounder
Center frequency	5150–5750 MHz	5300 MHz
Bandwidth	10–240 MHz	120 MHz
Tx-code length	1.6 μs	N/A
Sampling rate at Tx	320 MHz	N/A
Rx-element switching interval	3.2 μs	3.2 μs
Time between MIMO snapshots	39.3216 ms	39.3216 ms

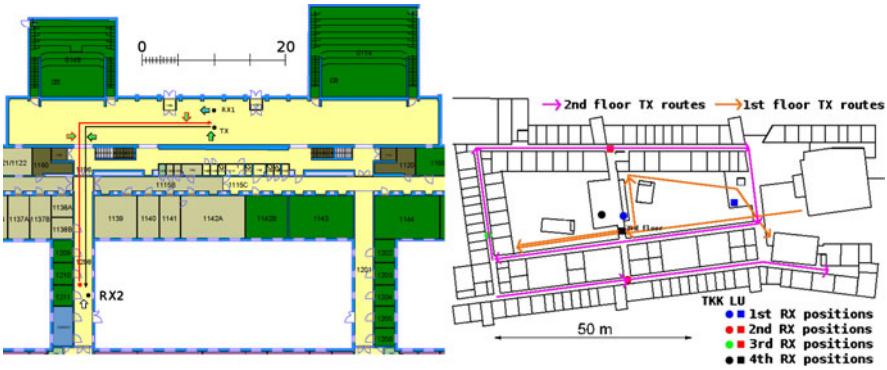

(a) (b)

Fig. 2.2 Scenarios of the WILATI measurements at (**a**) Lund University [KAK+07] (©2007 EurAAP, reproduced with permission). (**b**) Aalto University [RTR+08]

The receiver of the Aalto sounder consists just of a down converter and sampling unit. All the signal processing is done in a postprocessing step and was adjusted to cope with the LU transmitter's signals.

A special procedure for achieving synchronization between the different sounder architectures was necessary for this specific setup. A comparison of the sounder specifications is provided in Table 2.1. It is noteworthy that both sounders used calibrated antenna arrays, which enabled high-resolution estimation of the propagation paths in the channel, as discussed in Sect. 2.2.1. The indoor scenarios included dynamic measurements along routes on corridors (see Fig. 2.2a), and in big multistorey halls (see Fig. 2.2b).

A number of interesting findings resulted from these measurements. Most prominently, the analysis of the location of scatterers (see Fig. 2.30) lead to the investigation of common clusters (see Sect. 3.5.3.5). Additionally, interlink correlations were analyzed from the measurements in [KHH+10].

Outdoor Multiuser Measurements Eurecom employed their own equipment, the Eurecom MIMO Open-Air Sounder (EMOS), for outdoor measurements of multiuser MIMO channels [KKC+08]. The platform consists of a BS that continuously

Table 2.2 Eurecom EMOS sounder specification

Parameter	Eurecom EMOS
Center frequency	1917.6 MHz
Bandwidth	4.8 MHz
BS transmit power	30 dBm
Number of antennas (BS)	4 (2 cross-polarized)
Number of antennas (UE)	2
Number of OFDM subcarriers	160

sends a signaling frame, and one or more User Equipments (UEs) receive these frames to estimate the channel. For the BS, a PC with four PLATON data acquisition cards is used along with a Powerwave 3G broadband antenna. The UEs are ordinary laptop computers with Eurecom's dual-RF CardBus/PCMCIA data acquisition cards fed by two clip-on 3G Panorama Antennas (all antennas uncalibrated). While the platform is designed for a full software-radio implementation, it is also well suited for channel sounding. The parameters of this system are provided in Table 2.2.

The sounder is based on over-the-air synchronization and channel estimation by an Orthogonal Frequency Division Multiplexing (OFDM) sounding sequence. As shown in Fig. 2.3, one transmit frame is 2.667-ms long and consists of a synchronization symbol (SCH), a broadcast data channel (BCH) comprising 7 OFDM symbols, a guard interval, and 48 pilot symbols from a random QPSK sequence used for channel estimation. The subcarriers of the pilot symbols are multiplexed over the four transmit antennas to ensure orthogonality in the spatial domain.

A sample scenario investigated in these measurements was outdoor in a semiurban hilly terrain in Sophia-Antipolis, France. The base station was mounted on the rooftop of a building and four mobile stations were placed in passenger cars (see Fig. 2.4a). As an exemplary result, a comparison of the sum rate capacity of Single User (SU)-MIMO and Multiuser ((MU))-MIMO is given in Fig. 2.4(b). The results show that, both for measured and simulated channels, MU-MIMO provides a higher sum rate capacity than SU-MIMO Time-Division Multiple Access (TDMA).

These measurements also provide the basis for the investigations presented in Sect. 3.5.2.4. The EURECOM sounder was also extended to the 800 MHz band,

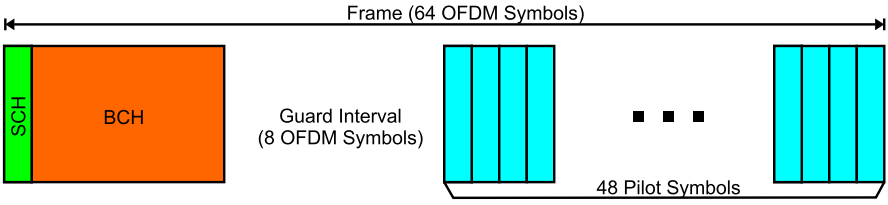

Fig. 2.3 Frame structure of the Eurecom MIMO OpenAir Sounder (EMOS) [KKC+08] (©2008 IEEE, reproduced with permission)

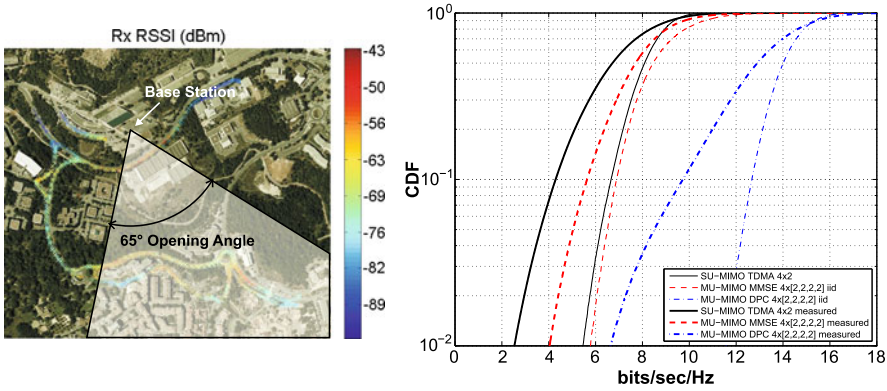

(a) (b)

Fig. 2.4 Outdoor multiuser MIMO measurements using the Eurecom sounder; (**a**) received signal strength in the scenario (©2008 IEEE, reproduced with permission). (**b**) Capacity of different multiuser MIMO communication schemes in this scenario [KKC+08]

in which it was used for the comparison of LTE transmission modes in rural areas [KGL+10].

Outdoor-to-Indoor Multiuser MIMO In this multiuser scenario, FTW and Stanford University used sequential measurements using a single-channel sounder [CBVV+08b]: They demonstrated that, given the *scenario* is static, multiuser measurements can be performed sequentially, even if the users themselves are moving [CBVV+08a].

As equipment, the RUSK Stanford Channel sounder produced by MEDAV GmbH [cha10] was used. The sounder architecture is similar to the Lund University equipment presented before. Additionally, a distance wheel was used to trigger the acquisition of MIMO snapshots every 1.6 cm of receiver movement. At the base station, two dual-polarized WiMAX base-station antennas were used as transmitters. At the receiver side, three types of commercial WiMAX dual-antenna MIMO arrays were used: a customer-premises equipment (CPE) array, a PC-card array, and a USB-stick array. Additionally, two discone antennas were used as reference array. The parameter settings of the measurements are provided in Table 2.3.

Figure 2.5(a) shows the map of the outdoor scenario with two Tx positions and the corresponding Tx locations. At every position, the BS was rotated into three different directions. Indoors, the measurements were done along five routes for each transmitter location and orientation as indicated in Fig. 2.5(b). These routes were maintained with meticulous precision (maximum deviation of 2 cm) to ensure the repeatability of the measurements. The indoor environment is a cubicle-style office, where the cubicles consisted of cardboard walls with metal frames. A glass wall was along Route 3, supported by a metallic structure.

It should be noted that the measurement data of this campaign is publicly available upon request [CBVV+08b].

Table 2.3 RUSK Stanford sounder specification for multiuser MIMO measurements

Stanford sounder parameters	MU-MIMO	O2I distr.	I2I static	I2I mobile
Center frequency	2.45 GHz			
Bandwidth	240 MHz (70 MHz used)			
Tx code length	3.2 μs			
MIMO snapshots spacing	1.6 cm = 0.13λ	250 ms	250 ms	9.8 ms
Number of antennas (BS)	4 (2 x-pol)	4 (2 x-pol)	8	8
Number of antennas (MS)	4 arrays × 2 ant.	8	8	8

(a) (b)

Fig. 2.5 Outdoor-to-indoor multiuser MIMO measurements [CBVV+08b]; (**a**) outdoor scenario (©2011 Google-Imagery ©DigitalGlobe, USDA Farm Service Agency, GeoEye, U.S. Geological Survey, MapData ©2011 Google), (**b**) indoor routes

To demonstrate the feasibility of the single-sounder approach, the channel matrices from two consecutive measurement runs along the same route were compared using the matrix collinearity measure (3.22).

Figure 2.6 demonstrates that the measured channels showed a strong collinearity in the distance range between 5 and 10 meters when the measurements of the two runs were properly aligned with each other. When using the collinearity measure on the channel *correlation matrices* (instead of the channel matrices), a high collinearity (larger than 0.9) is achieved throughout the whole measurement route. This demonstrated that, by appropriate measures, the environment was sufficiently static to perform multiuser channel measurements with just a single-channel sounder.

These measurements were used to derive and analyze a subspace-based model of the multiuser MIMO channel (see Sect. 3.5.2.1).

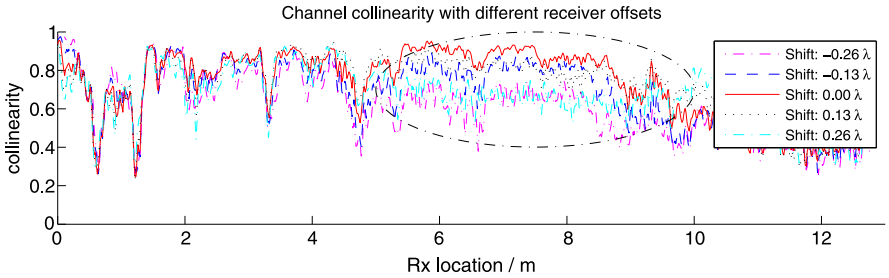

Fig. 2.6 Validation of doing multipass measurements: The channels matrices are collinear over a longer range when the environment does not change between runs [CBVV+08a]

Outdoor-to-Indoor and Indoor-to-Indoor Distributed Nodes Two similar measurement campaigns of the radio channel between indoor nodes distributed throughout a building and between the nodes and an outdoor base station were first presented in [CBVV+08b] (US-style office building with cubicles) and were succeeded by a follow-up campaign [CCL+10] (European-style office building with brick-walls).

The basic idea in both campaigns was to use a single switched-array channel sounder but connect long low-loss RF cables to the RF switches. In this way, the measured antenna "array" consisted of the antennas at the distributed nodes. Naturally, this approach results in a lower measurement SNR due to the cable losses, which needs to be compensated for in a postprocessing step.

The measurements in [CBVV+08b] were performed with the RUSK Stanford channel sounder produced by MEDAV GmbH [cha10]. Three different scenarios were measured: (i) outdoor-to-indoor (O2I) static, (ii) indoor-to-indoor (I2I) static, and (iii) I2I mobile. The sounder parameters for each of the measurements are provided in Table 2.3.

The scenario is shown in Fig. 2.7(a). Both static and mobile measurements were performed. In the static measurements, the antennas were at fixed positions while fading was generated by people that were moving throughout the room. For the mobile measurements, specific antennas were moved locally. From these measurements a comprehensive O2I and I2I model for distributed channels was designed [OCB+10].

The follow-up campaign presented in [CCL+10] was using an Elektrobit Propsound CS channel sounder [Ele10, HKY+05]. This sounder is also a switched-array MIMO channel sounder but using pseudorandom sequences for probing the channel. At the receiver, a matched-filtered impulse response can be obtained by postprocessing.

In this campaign a larger number of static and mobile scenarios were measured, both outdoor-to-indoor and indoor-to-indoor. Additionally, indoor nodes were occasionally equipped with multiple antennas. An exemplary map of indoor measurements is depicted in Fig. 2.7(b).

From these measurements a statistical model for outdoor-to-indoor and indoor-to-indoor distributed links was developed [OCB+10] (cf. Sect. 3.5.4.2).

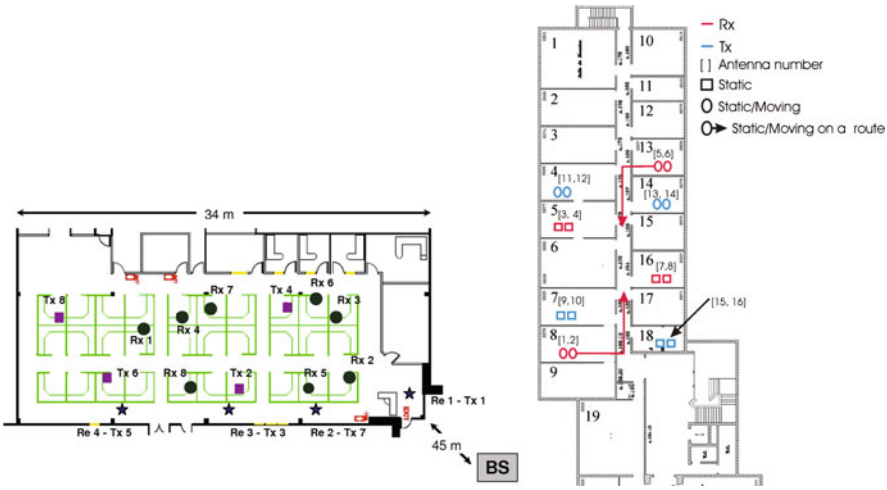

(a) (b)

Fig. 2.7 Distributed node measurement scenarios: (**a**) Stanford campaign—*black dots* denote receivers (O2I & I2I), *stars* denote "relays" (Rx for O2I, Tx for I2I), and *squares* denote transmitters (I2I) [OCB+10] (©2010 IEEE, reproduced with permission). (**b**) UCL campaign [CCL+10]—exemplary measurement

Outdoor Relay Channel An intermediate step toward the measurements of multiple base stations was performed by Bristol University [WWW+07]. In their study, they considered a realistic environment of outdoor BS-to-relay and relay-to-UE channels, as addressed in the IEEE 802.16j standard for WiMAX relaying. Both at the BS and at the Relay station, two signal generators were used, transmitting a CW at 3.59 GHz and 3.47 GHz, respectively. As UE, a spectrum analyzer was used to quantify the propagation loss for both frequencies. The UE was mounted on a trolley and pushed along several routes to collect samples for estimating the path loss. For the path loss on the BS-UE link, the COST 231 Walfish–Ikegami model was found to provide the closest match to the measured data. For the relay-UE link, the conventional models are farther off, which implies that the development of models with more localized parameters is called for. Finally, the BS-relay link showed a tight fit to the IEEE 802.16d [IEE04] model, with deviations due to the antenna heights.

Orange Labs [CCC10a, CCC10b] performed two extensive studies where they included the outdoor-to-indoor link. In their first study [CCC10a], a narrowband signal was used as well, but at three carrier frequencies (900 MHz, 2.1 GHz, and 3.5 GHz). The signal was transmitted from a roof of a 21-m high building in an urban environment. The receiver was placed at different floors (outdoors and indoors) of a close-by 5-floor building. The distance between Tx and Rx was about 150 meters.

Their second study [CCC10b] focused on the path loss between base station and relay station. The base station was mounted on the roof of a 20-m high building. An extensible antenna was mounted on a van to simulate relay stations with different

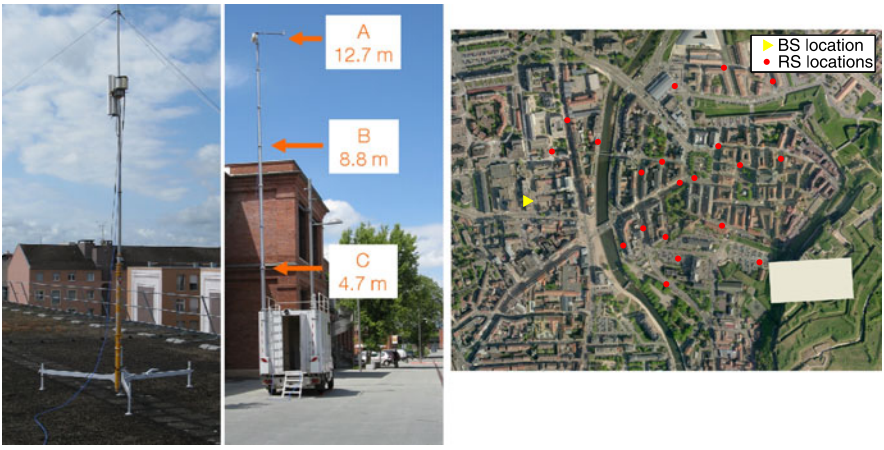

Fig. 2.8 Relay measurements in Belfort, France [CCC10b]; *Left*: Photo of base station and relay station with 3 antenna heights; *Right*: Map of the environment

height. The measured points for the relays were distributed throughout the city center of Belfort, France. The antennas and measurement map are shown in Fig. 2.8. In both studies, narrowband transmitters and receivers were used.

The measurements demonstrated that in general, a higher floor provided more power for all considered frequencies. It was found that the corresponding WINNER feeder-link models for LOS (B5a) was consistent with the measurements. For the NLOS model (B5f), higher deviations are observed for the receiver at lower floors. However, the model was based on the assumption that NLOS receivers are on high floors, which explains the deviations.

More details on the path loss results and fitting path loss models are provided in Sect. 3.1.

Outdoor Peer-to-Peer Channel In [ETM07], the authors measured an outdoor peer-to-peer channel at 300 MHz. MIMO at such a low carrier frequency is attractive for peer-to-peer communications because it combines the good coverage of a low-carrier-frequency system with the high data rates enabled by MIMO.

The measurements were performed using the RUSK LUND channel sounder using uniform circular dipole arrays mounted to the roof top of two cars. The measurements took place in a rural/semi-suburban area near Linkoping, Sweden, showing groups of trees and buildings in the environment.

The evaluation of these measurements are presented in Sect. 3.5.4.1.

2.1.1.2 Multibase-Station Measurements

Although single-base-station channel measurements are commonplace today, they involve an appreciable effort to accomplish. The increased complexity of perform-

Table 2.4 TU-Ilmenau sounder specifications

Parameter	TU-Ilmenau RUSK sounder
Center Frequency	2.53 GHz
Bandwidth	2×40 MHz
CIR length	6.4 µs
Transmit power	46 dBm
MIMO Snapshot rate	75 Hz
Number of BS	3
Inter Site Distance	580–680 m
BS antenna	16 ULA (8 cross-polarized)
UE antenna	48 cylinder (24 cross-polarized) + 10 (MIMO-Cube)

ing multibase-station channel measurements implies an extraordinary challenge explaining the fact that those campaigns are relatively rare.

One straightforward way to accomplish multibase-station measurements is to repeat a specific UE measurement route using different single sites in sequence. The drawback is that the work load increases proportionally to the number of base station sites. Nevertheless, this method has been employed in MIMO multilink campaigns in three cities in Germany using Medav RUSK channel sounders. GPS in combination with odometers are used to make sure that sufficient UE position accuracy is kept when the same route is repeated for the different sites. In a campaign performed by the Technical University of Ilmenau [NKS+09] within the EASY-C project, three base station sites (see Table 2.4) were placed in the center of Ilmenau at different heights using a sky lift. First investigations were done on the large-scale parameters with the results that multipass measurements are possible even in suburban environments under certain precautions [NKJ+10].

The campaigns in Berlin and Dresden were also performed within the EASY-C EU project. Different scenarios (see Table 2.5) with intersite distances between 100 m and 700 m were employed. The gain of cooperation between the sites has been evaluated in a scenario with five mobile users and four base station cites at the Technical University of Berlin (TUB) campus [JJT+09]. A five-fold gain in cell throughput is obtained as shown in Fig. 2.9.

In a measurement campaign performed by Ericsson Research [LMF10] simultaneous coherent transmission from three different base station sites was accomplished by means of fiber optical distribution on the RF signal to each antenna at each site. A map of the measurements is shown in Fig. 2.10. The Ericsson channel sounder is based on their own developed MIMO testbed for LTE. In this campaign a single Kathrein base station antenna was used at each site. Details of the setup is provided in Table 2.6. The measured channel data were used to investigate the gain of multibase-station coherent cooperation in a single-user scenario. A convenient measure of the MIMO performance of the channel is the eigenvalue dispersion σ_λ according to

Table 2.5 EASY-C project sounder specifications

Parameter	Berlin	Dresden	TUB (Berlin)
Center Frequency	2.53 GHz	2.53 GHz	5.2 GHz
Bandwidth	20 MHz	21.25 MHz	120 MHz
BS/Sectors	3/3	3/3	4/1
Transmit power	41 dBm	41 dBm	40.3 dBm
MIMO Snapshot rate	500 Hz	1150 Hz	500 Hz
BS antennas	ULA 16	Kathrein 2	Star 16
UE antennas	Cube 10	CUBA 16	Cube 10
Inter Site Distance	500 m	750 m	100–200 m

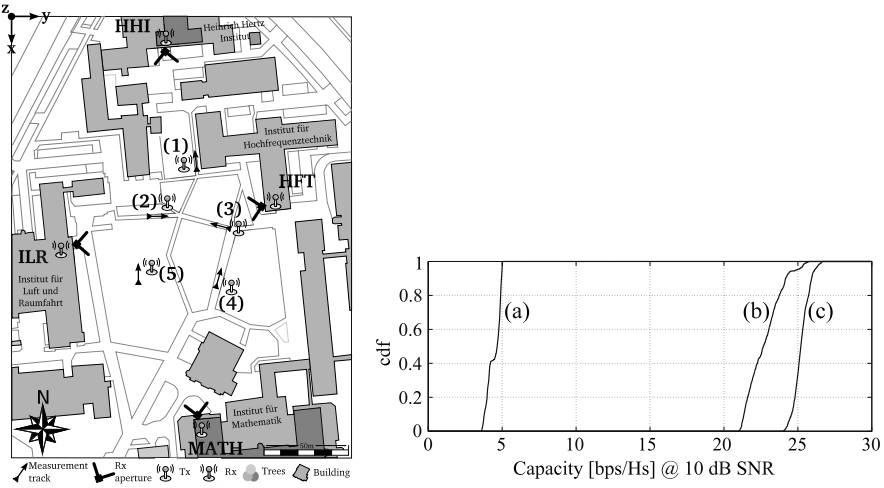

Fig. 2.9 *Left*: Campus map of the TUB. BS locations are indicated by the short names of the institute buildings. The five short measurement tracks are indicated by *arrows* [JJT+09] (©IEEE 2009, reproduced with permission). *Right*: Distributions of capacity for the traditional deployment with different resources in each cell (*a*), mean capacity of isolated cells (*b*) and capacity with base station cooperation using a common resource (*c*), all for SNR = 10 dB [JJT+09] (©IEEE 2009, reproduced with permission)

$$\sigma_\lambda = \left(\prod_{i=1}^{N} \lambda_i\right)^{1/N} \Bigg/ \left(\frac{1}{N}\sum_{i=1}^{N} \lambda_i\right). \tag{2.1}$$

σ_λ may take values between 0 and 1 where 0 corresponds to fully correlated antennas and 1 to the best possible MIMO channel in the sense that all eigenvalues are equal. In the case of a 2×2 system, $\sigma_\lambda \approx 0.6$ for an i.i.d. Rayleigh fading channel. Figure 2.10 shows the distributions of σ_λ together with the average channel gain for the three base station sites. It is clear that the best MIMO performance is obtained in areas between the three sites where the signal strengths are similar.

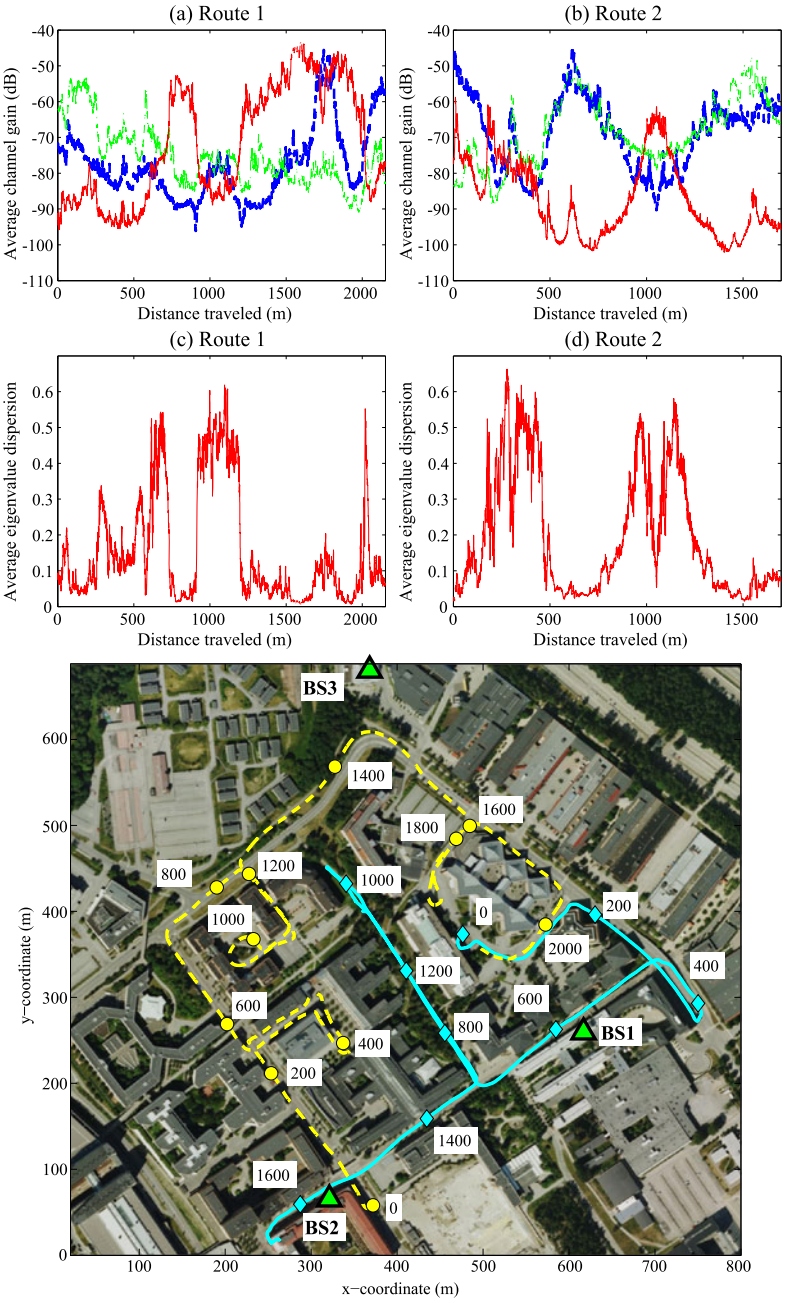

Fig. 2.10 Simultaneous channel measurements with multiple base stations. *Top*: Average channel gain per receive antenna over 20 MHz for BS 1 (*blue*), BS 2 (*green*), BS 3 (*red*) for (**a**) route 1 and (**b**) route 2. Average eigenvalue dispersion for (**c**) route 1 and (**d**) route 2 [LMF10] (©IEEE 2010, reproduced with permission). *Bottom*: Location of BSs and route 1 (*yellow*) and route 2 (*cyan*) of MS. Distances from starting points are indicated in meters

Table 2.6 Ericsson sounder specifications

Parameter	Ericsson sounder
Center Frequency	2.66 GHz
Bandwidth	19.4 MHz
CIR length	22.2 μs
Transmit power	36 dBm
MIMO Snapshot rate	190 Hz
Number of BS	3
Inter Site Distance	580–680 m
BS antenna	1 Kathrein (18 dBi 45 deg polarized)
UE antenna	2 dipoles + 2 magnetic loops

Additionally, it was shown that—using the coherent measurements—the mobile nodes' location could be well estimated [MSKF10].

2.1.2 Polarimetric Channel Measurements

With increasing interest in multiantenna communications over the past decade, the polarimetric behavior of the radio channel is investigated intensively. A lot of experiments have been conducted in order to improve the understanding of the polarized radio channel. In order to determine the polarized electromagnetic field fully, its vector components have to be measured. This may be achieved by means of a tripole antenna which measures all three field components at one point in space. For radio channel modeling, it is, however, convenient to decompose the electromagnetic field into a set of plane waves. A plane electromagnetic wave is fully characterized by the two field components which are perpendicular to its direction of propagation (the corresponding longitudinal component vanishes). In channel measurements each plane wave is typically characterized with the horizontal and polar (vertical in the case of propagation in the horizontal plane) field components.

There are two basic metrics for statistical characterization of the polarization properties of measured channels. The first is the cross polar discrimination (XPD), i.e., the power ratio between co-polar and cross-polar transmission and reception (P_{VV}/P_{HV}, P_{HH}/P_{VH}). The second is the copolar power ratio (CPR), i.e., the power ratio between the two copolar transmission and reception cases (P_{VV}/P_{HH}).

In [QCOD07, QOHD08b] the polarization characteristics in an indoor corridor-to-room scenario have been measured. At the transmitter location in the corridor two log periodic vertically and horizontally polarized antennas were used. At the receiver locations in the room a tripole antenna was used. To determine the direction of each incoming wave at each receiver location a Bartlett beamformer, based on a two-layer horizontal planar virtual array each of 10×10 elements, was used. Here the observed XPD was around 10 dB. Interestingly, the authors derived in

Table 2.7 Sounder specifications and channel polarization XPD and CPR for the different polarization campaigns

Parameter	[DC08]	[QOHD08b]	[KMGT09]	[PQD+09]	[MGPRJL08]
Center Freq.	2.2 GHz	3.6 GHz	4.5 GHz	3.5 GHz	2.45 GHz
Bandwidth	62.5 MHz	200 MHz	120 MHz	CW	200 MHz
BS antenna	VH	VH Log-periodic	VH planar $2 \times 4 \times 2$	VH	4 monopoles
UE antenna	VH Omni	Tripole	VH circular $(2 \times 24 \times 2)$	Tripole	4 monopoles
Scenario	Urban Macro	Corridor-to-room	Urban Macro	Indoor + Outdoor-to-indoor	indoor
XPD	5 dB	10 dB	9 dB	5 dB	8–16 dB
CPR	3 dB	NA	-1 dB	-2 dB	NA

[QOHD08a] analytically that the XPD should fit an F-distribution for Rayleigh and Ricean fading, which is also supported by measurements.

A somewhat lower observed channel XPD around 5 dB was observed in [PQD+09] in an indoor scenario and outdoor-to-indoor scenario. The CPR was around -2 dB.

In an urban macro-cellular campaign in Mulhouse [DC08] the polarized radio channel was measured at 47 UE locations. The average XPD of the measured channel is around 5 dB. Comparing the gains between the copolar transmission modes, a 3 dB effect of lower loss for vertical polarization is observed (CPR = 3 dB). These findings are also supported by the Ilmenau multibase campaign [SSN+09] where the XPD and CPR were measured (in the same type of scenario) to about 7 dB and 3.5 dB, respectively.

Another urban macrocellular campaign was performed by Tokyo Institute of Technology [KMGT09]. Here a circular stacked double polarized array was used at the UE. For the polarimetric analysis, the RIMAX superresolution method was used.

The vertical to horizontal cross-polar discrimination (XPD) of the radio channel ranged from about 5 dB to about 10 dB. The corresponding CPR was -1 dB, which is in contrast to the other two macrocellular campaigns [DC08, SSN+09].

A polarized MIMO indoor campaign was carried out by [MGPRJL08] using a 4×4 system of monopole antennas. To capture different polarizations, the antennas were rotated between measurement runs. Depending on the environment, the authors observed XPDs between 8 and 16 dB.

Investigations of polarized MIMO in a tunnel [LSD+09] showed that the XPD increases, as soon as the distance between Tx and Rx becomes larger than few times the tunnel width (or height). An overview of the sounder specifications for all the measurements presented are provided in Table 2.7.

2.1.3 Vehicular Channel Measurements

2.1.3.1 Measurement Practice

Vehicular propagation channels can be separated into Vehicle-to-Vehicle (V2V) and Vehicle-to-Infrastructure (V2I) channels, and are typically highly dynamic since one or both link ends can move at very high speeds. A lot of the research that has been conducted in this area was sparked by international standardization work envisioning intelligent transport systems in the 5.9 GHz band (e.g., IEEE 802.11p [WAV]).

Measurements of propagation channels for vehicular systems put high requirements on the measurement equipment. The mobility of the link end(s) in such systems implies high Doppler shifts which the channel sounder needs to cope with by means of very fast sampling. V2V channels are particularly challenging, since, in contrast to cellular systems, Tx and Rx are at the same height, which results in multiple scattering around both link ends. Furthermore, there are many important scatterers moving at high speeds, which combined with the mobility of Tx and Rx even can result in propagation channels that are nonstationary [PZB+08]. The high mobility and challenges of measuring V2V propagation channels can be demonstrated by considering a Tx and Rx that are driving in convoy at a speed v. A multipath component that is generated by a single bounce off another vehicle driving at the same speed toward the Tx/Rx convoy will then have a Doppler shift of $\nu = 4 f_c v/c$ (where c is the speed of light). For a center frequency $f_c = 5.9$ GHz and a speed $v = 110$ km/h, this results in a Doppler shift of 2.4 kHz.

The vehicle-to-vehicle measurement campaigns within COST 2100 have used different parameter settings in their measurement setups, particularly concerning the size of the MIMO system and the vehicle speed. In [RKVO08] and [RKVO10], large MIMO systems were measured (30×30 and 30×4, respectively) while using a low driving speed of the Tx and Rx cars (5–20 km/h). The measurements in [PKC+07] and [PKZ+08], on the other hand, were conducted at speeds up to 110 km/h but involved a much smaller MIMO system (4×4).

The V2I measurements in [PKH+08], which characterized the propagation channel between a base station and a high-speed train (260–290 km/h), deployed a 16-element array at one link end and a single antenna element at the other. These measurements were performed in two steps: First the antenna array acted as base station, and the single antenna was used as mobile unit. Then, the measurement was repeated with the reversed situation. In this way, directional information could be extracted at both sides (though, strictly speaking, double-directional data is neglected).

The parameter settings for the V2V measurement activities within COST 2100 are summarized in Table 2.8. It is noteworthy that no campaign has been conducted at 5.9 GHz as suggested by standards [WAV], usually for regulatory reasons or due to limitations in the measurement equipment. The difference between channel characteristics at the measured frequency bands and 5.9 GHz are commonly expected to be negligible [PKC+07, RKVO08, PBK+10, RKVO10].

One aspect that requires special attention in V2V channel measurement campaigns is their documentation, most importantly of the Tx and Rx (spatial) coordinates. Whereas it is simple to obtain these coordinates for measurements where

Table 2.8 Measurement parameters in vehicle-to-vehicle measurement campaigns within COST 2100

	[PKC+07]	[MFP+08]	[RKVO08]	[PBK+10]	[RKVO10]
Center freq. [GHz]	5.2	5.2	5.3	5.6	5.3
Bandwidth [MHz]	240	120	120	240	60
Snap. rep. [ms]	0.3072	1/10	8.4	N/A	15
Tx power [dBm]	27	33	36	27	36
Tx antennas	4	1	30	1/4	4
Rx antennas	4	1	30	1/4	30
Vehicle speed [km/h]	30–110	10/90	5–15	N/A	5–20
Snapshots	32500	N/A	967–2006	N/A	N/A
Recording time [s]	10	10	67–140	N/A	N/A
Tx ant. height [m]	2.4	roof + 0.2	2.12	N/A	N/A
Rx ant. height [m]	2.4	roof + 0.2	2.32	N/A	N/A

both link ends are static, or one is moving at a moderate speed, the fast sampling and high speeds make the acquisition less feasible in V2V measurements. For directional estimation analysis of measurement data, this is especially important. Even though exact knowledge of the Tx and Rx coordinates is not necessary for extracting directional estimates, it is still essential for their interpretation; without such knowledge the mapping of the extracted results to physical scattering objects is impossible. The usual way of conduct is to use GPS receivers at Tx and Rx in order to log their time-varying coordinates [PKC+07, PBK+10, RKVO10]. GPS data, however, can suffer from inaccuracies due to multipath propagation, especially in urban environments, and may for this reason be supplemented by video documentation [PKC+07]. An alternative approach was used in [MFP+08], where the Tx car was kept static while the Rx car was moved at a low speed (10 km/h). The aim here was to verify a raytracing model and simultaneous track-keeping of two vehicles was deemed to inaccurate for such purposes.

The characteristics of propagation channels depend on the particular propagation environment and measurement data is therefore usually classified into several well-known environments. For V2V channels, the most common are highway, urban, rural, campus, and suburban [PKC+07, MFP+08, RKVO08], which differ in, inter alia, scatterer densities, (road) geometry (lane width, number of lanes etc.), and roadside objects (houses, sound abatement walls, metal fences, etc.). However, there are also some additional classification concerns that are of importance for V2V propagation channels. First, the distinction between LOS and NLOS is not straightforward since shifts between the two situations may occur rapidly due to the sudden obstruction by, e.g., a truck. One measurement method is to let the Tx and Rx drivers apply a "realistic" driving behavior [RKVO08] and let the channel conditions shift naturally between LOS and NLOS, but dedicated measurements where the LOS is deliberately obstructed by letting a truck drive between Tx and Rx have also been conducted in order to isolate the effect of LOS obstruction [PBK+10]. Second, it is

common to distinguish between measurements where the Tx and Rx cars are driving in the same direction [PKC+07, RKVO08, MFP+08] and measurements where the direction of travel is the same [PKC+07, RKVO10] since the channel properties can be significantly different in those situations (e.g., in terms of Doppler shifts). Third, in the context of traffic safety applications, it is of interest to characterize propagation channels for the particular traffic situations that are important for such applications, e.g., precrash applications such as intersection collision avoidance. For such purposes, the regular environment classification (highway, urban, etc.) is not sufficient, and therefore measurements have also been conducted in intersections [PBK+10], traffic congestion [PBK+10], and overtaking situations [RKVO10].

2.1.3.2 Choice of Vehicles and Antennas

In any measurement campaign, the choice of antennas (or antenna arrays) is important and will impact the end result. For vehicular channel characterization, the type of vehicle that is used and the location of the antenna on the vehicle will also largely impact the result. The antenna location on a given vehicle not only affects the influence from the subject vehicle, but also how much influence other vehicles and scatterers will have on the received signal. The impact of antenna location on system performance was investigated through simulations in [RPZ09] but has not yet been analyzed by measurements.

In vehicular measurements, the most common approach is to use a "regular" antenna array (i.e., an antenna array specially designed for channel characterization) mounted at an elevated position on the vehicle (usually on/above the vehicle roof) [PKC+07, MFP+08, RKVO08, RKVO10] or inside the vehicle [PKH+08]. Examples of regular antennas include a monopole [MFP+08], a uniform circular array [PKC+07, PKH+08], or a semi-spherical array [RKVO08, RKVO10]. Such an approach leads to a straightforward characterization of the propagation channel, but the elevated position reduces the possibility of obstruction of the LOS and other important propagation paths, and may thus lead to an overly beneficial channel. An alternative is to use an antenna array specially designed for vehicular applications, thus constituting a realistic example design that could be used by a commercial V2V communications system [PBK+10]. This leads to a channel that is realistic from an application point-of-view, though the generality of the results can be limited by the particular antenna arrangement that is used.

2.1.3.3 Performance Analysis of 802.11p Vehicle-to-Infrastructure Links

The usual goal of channel measurements is to obtain a description of the channel transfer function, or conversely, the channel impulse response. However, channel measurements can also be conducted in order to assess the performance of a particular wireless system. In [PTA+10], the performance of the physical layer in the IEEE 802.11p standard was investigated by means of V2I measurements. The goal

was to characterize the average downstream packet broadside performance for a vehicle passing two road side units. The road side units were mounted on top of a highway gantry and the van had an onboard unit mounted on top of it. The measurements were conducted by disabling the retransmission function of the MAC layer, filling the MAC service data unit of the transmitting road side units with random data (of a specific length) and then continuously transmitting these data while the van was driving along the highway at 80 km/h or 120 km/h. After reception, it was determined whether the frames where correctly decoded by the receiving onboard unit.

2.1.4 UWB Channel Sounding

Ultra-WideBand (UWB) channel sounding requires equipment that is capable of handling the ultrawide frequency bands under consideration. This section describes measurement efforts in the 3.1–10.6 GHz band, the frequency range allocated in the US by the FCC for unlicensed use of UWB systems [FCC02]. Only subsets of this band may be available in other parts of the world, or of interest for certain applications, therefore some measurement campaigns address only parts of these frequencies.

Vector Network Analyzer (VNAs) that cover this frequency band are available in many labs and have therefore been used in many UWB measurement campaigns [Mol09, ASQ09]. VNA-based measurements have also been presented to this COST action by various groups (see Sect. 6.3.1) and already to the predecessor action COST 273 (see [Cor06]). The VNA's key advantages are a large dynamic range and a (rather) free and flexible choice of the measurement band. Its key disadvantages are the required RF cables to connect the VNA to the TX antenna *and* the RX antenna, and the relatively slow measurement speed due to the sequential scanning of the frequency points. The latter is fortunately less critical in many cases, since UWB communications is mostly limited to indoor applications by regulation, where one can often make sure that there are no moving objects in the environment. But it prevents—on the other hand—characterization of time variations of the channel.

This section describes alternative measurement equipment that has been employed in UWB channel measurements presented within COST 2100. We first address a Pseudo Noise (PN) Direct Sequence Spread Spectrum (DSSS) channel sounder that has been used by the authors of [CPB07, CTB08]. The channel sounder better supports dynamic channels, as it simultaneously measures the complete frequency band. The second topic of this section is a demonstrator system for the standardized IEEE802.15.4a UWB signaling scheme that has been discussed in [GBG+09, GBA+09, AAM09]. The IEEE802.15.4a standard defines preamble sequences that are designed for estimating a channel impulse response at fine time resolution in order to support robust ranging and positioning in indoor applications [IEE07]. Its signal scheme is thus well suited for UWB channel sounding.

Note that the results of the measurement campaigns are described in Sect. 6.3.1; this section only details the measurement technology. For an overview of the measurement campaigns, please refer to Table 6.6.

2.1.4.1 Time-Domain Channel Sounding

Two methods are commonly used for time-domain channel sounding, which differ by the type of RF signal used. One method is based on transmission of short "isolated" pulses that yield at the receiver directly the channel's impulse response (convolved with the pulse shape of the probing signal). The time resolution is determined by the bandwidth of the transmitted pulse, i.e., the pulse duration. Unfortunately, the pulse energy decreases with increased bandwidth such that the resulting sounding signal—a low-duty-cycle pulse stream—has very low power. As a consequence, high pulse voltages are needed at the transmitter, and demanding specifications result for the receiver to offer sufficient dynamic range and sensitivity.

The second method is based on PN sequences as sounding signals, and it bears the advantages of DSSS systems. In stead of isolated pulses, PN sequences of digital symbols are transmitted. The continuous transmission increases the average power of the transmitted signal, while the bandwidth is still determined by the bandwidth (duration) of the (baseband) pulse used for modulating the PN sequence. The receiver performs correlation processing to determine the channel impulse response in time domain. It thereby exploits processing gain proportional to the time-bandwidth product of the PN sequence [BLM04, Pro95], which quantifies the energy gain with respect to the method using isolated pulses. Correlation processing also suppresses (narrowband) interference signals, another important advantage of this technique.

2.1.4.2 M-Sequence UWB Channel Sounding

A channel sounder based on an Maximum Length Binary Sequence (MLBS) has been used in the measurements presented in [CPB07]. The channel sounder [KSP+05, SHK+07] generates a length-4095 MLBS by using a shift register clocked at 7 GHz. Up-converting the obtained baseband signal to a 7 GHz (synchronous) carrier provides a sounding signal covering the 3.5–10.5 GHz band, which agrees reasonably well with the frequencies allocated by the FCC. The sequence repeats after roughly 600 ns, which determines the maximum channel excess delay that can be measured unambiguously. This is sufficient for common indoor UWB channels. On the other hand, the short sequence length allows for subsampling to simplify the receiver hardware. A subsampling by a factor of 512 still allows for the acquisition of more than 3000 CIRs per second, while the sampling rate is reduced to a moderate speed of 13.7 MHz. Of course, subsampling means that a large amount of signal power is lost. Further details on the sounding architecture can be found in [KSP+05].

Calibration is a key step for ensuring accurate channel measurements. In case of the MLBS channel sounder, the data post processing includes suppression of

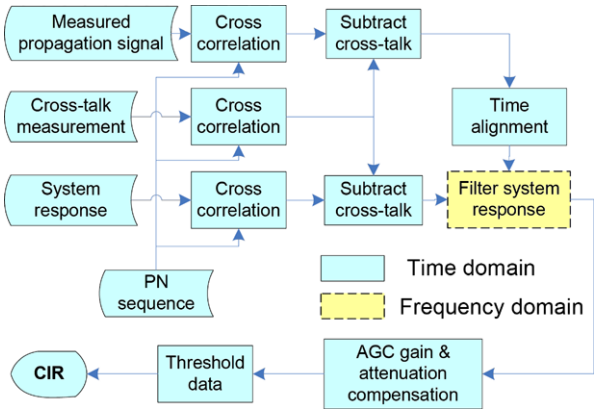

Fig. 2.11 Postprocessing of measurement data [CPB07] (©2007 IEEE, reproduced with permission)

crosstalk between the transmitter and the receiver, and calibration for the system response of the measurement equipment. Figure 2.11 illustrates the required signal processing steps [CPB07]. Cross-correlation with the MLBS is the first operation performed upon the acquired raw data. The crosstalk is measured with the receive port disconnected. It is also cross-correlated with the MLBS and then subtracted from the input data and the system response. The system response is measured with the transmit and receive ports connected directly. Finally, the system response is removed from the channel data by division in the frequency domain, where one has to take care to avoid noise amplification [CPB07].

The accuracy of the captured channel data was verified by comparison to measurements performed with a VNA. For that purpose a completely static, artificial multipath environment has been created inside an anechoic chamber [CPB07]. A close match has been observed within the frequency band of interest. In summary, the paper [CPB07] concludes, that "the time-domain sounder offers rapid data acquisition of real-time channel data at the expense of increased processing complexity and reduced dynamic range."

2.1.4.3 Channel Sounding Using IEEE 802.15.4a Preamble Signals

The preamble of the standardized IEEE 802.15.4a UWB signaling scheme [IEE07] starts with a code sequence that has ideal properties for channel sounding. Its autocorrelation shows a single peak at zero-shift and zeros otherwise, i.e., it is perfectly flat in the frequency domain, which means that it can probe any frequency (occupied by the signal) equally well.

In the IEEE 802.15.4a preamble ternary codesequences of length 31 or 127 are used to achieve such properties. That is, the chips of the preamble are taken from the set $\{-1, 0, +1\}$. Each chip is modulated by a baseband pulse with a bandwidth between 500 MHz and 1.5 GHz and then modulated on an RF carrier that sits at predefined channels within the UWB band. The spacing between consecutive preamble pulses is extended by a factor of 4, 16, or 64 with respect to the nominal pulse repetition frequency of 499.2 MHz, which stretches the period of the ternary code to

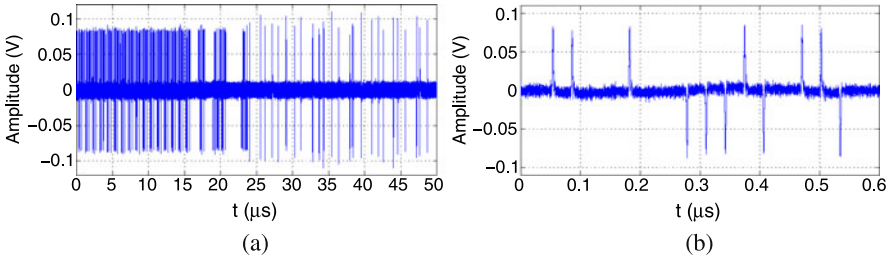

Fig. 2.12 (**a**) IEEE 802.15.4a signal in baseband. The cyclically repeated preamble is terminated by a start-of-frame delimiter, which is followed by pulse-position-modulated data symbols [GBA+09] (©IEEE 2009, reproduced with permission). (**b**) Close-up on the ternary preamble sequence [GBA+09] (©IEEE 2009, reproduced with permission)

about 1 or 4 μs, depending on the parameter settings. Finally, the ternary sequences are periodically repeated up to 4096 times, to increase their energy and to simplify code acquisition. The allowed parameter combinations can be found in the standard [IEE07]. Figure 2.12 shows an IEEE 802.15.4a signal with a close-up on the preamble sequence. Sixteen cyclic repetitions of a length-31 sequence can be seen with a pulse spacing extended by a factor of 16 to 32 ns.

The ternary code has the special property that its absolute value shows perfect cross-correlation properties with the original code sequence. Therefore simple energy detection receivers can also perform channel estimation [LCK06] and thereby exploit processing gain, albeit suffering from so-called noncoherent combining loss [GTPPW10].

Due to these code properties, IEEE 802.15.4a nodes are suitable for channel sounding within the frequency band they are operated at. This has been presented in [GBG+09, GBA+09, AAM09], using a standard-compliant demonstrator transmitter. The demonstrator, see Fig. 2.13(a), uses fast serial IO-ports of a Xilinx Field Programmable Gate Array (FPGA), so-called Multi-Gigabit Transceivers (MGTs), to generate the baseband sequence. Two MGT outputs are combined to obtain the ternary code symbols. The baseband signal is lowpass filtered for pulse shaping [AFG+09] and then up-converted to the carrier frequency, using either a Vector Signal Generator (VSG) as shown in the figure or a custom-designed up-converter [AGFW09, AAM09]. At the receiver side, the demonstrator acquires the received UWB signal directly with a real-time scope, a suitable bandpass filter, and an Low-Noise Amplifier (LNA). Any post processing is done offline. Clock synchronization of the FPGA, the VSG, and the scope simplifies this postprocessing, as the chip and sampling clocks then have a fixed phase relation, avoiding clock offset estimation and correction. Coherent processing of the UWB data yields channel impulse responses at high dynamic range as illustrated in Fig. 2.13(b). The real-time sampling supports measurements in time-variant environments. However, transferring the data to the PC is rather time consuming, therefore a real-time observation of channel variations is hard to achieve.

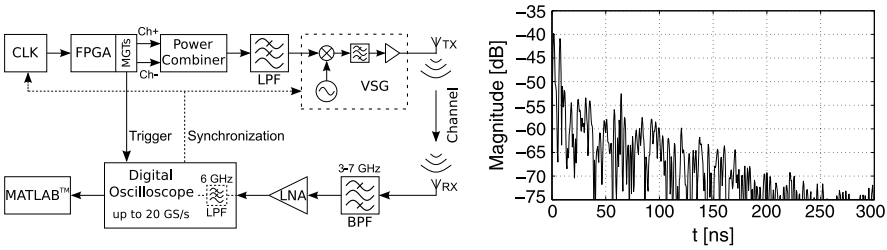

Fig. 2.13 (**a**) Demonstrator transmitter for the IEEE802.15.4a standard [GBA+09] (©IEEE 2009, reproduced with permission). (**b**) Channel impulse response captured in an industrial environment [GBA+09] (©IEEE 2009, reproduced with permission)

2.1.5 Millimeter and Submillimeter Waves

Wireless systems at millimeter-waves (mm-W) and sub-millimeter-waves (sub-mm-W) are promising solutions to reach broadband data rates for short-range communications [Smu02]. However, the realization of multi-Giga-bit/s data transmission at such frequencies becomes a challenge: about 3 Gb/s will be required for High-Definition (HD) uncompressed video [SOK+08], and similar rates are foreseen for PC connectivity and peer-to-peer communications. If this goal is achieved, the mm-W/sub-mm-W solutions will reduce the number of wires over our desks, TV rooms, and also within cars and aircraft cabins.

These new technologies are being developed in parallel with IEEE standards, i.e., 802.15.3c [IEE09] and 802.15.11ad [IEE10]. In Europe, the standard ECMA-387 has been defined for mm-W [ECM08]. Globally, about 7 GHz of unlicensed bandwidth (in some cases 9 GHz from 57 to 66 GHz) have been allocated, e.g., [FCC01] and [ECC03], which has increased the industrial interest. This is the highest amount of free spectrum assigned so far for short-range applications. Nowadays wireless multi-Giga-bit/s systems are being developed in some industrial projects in Europe, e.g., the *EASY-A* project[1] (Enablers for Ambient Services and Systems, Part A—60 GHz Broadband Links) or the MEDEA+ project *Qstream* (Ultrahigh-data-rate wireless communication). Massive markets include HD-TV home-cinema [SOK+08], office/meeting room point-to-point high-data-rate communications [JK09, JMK10], in-car/cabin point-to-multipoint video streaming [GKZ+10], real-time video streaming in medical applications [KSH+10, KHS+10], and fixed point-to-point radio links [GKKV10] (see some scenario examples in Fig. 2.14). Recently, public transportation scenarios have also been proposed for IEEE standardization at 60 GHz [Gar10].

In this context, this section addresses measurements and characterization of mm-W and sub-mm-W channels. There are still many open questions about the

[1] URL: http://www.easy-a.de/.

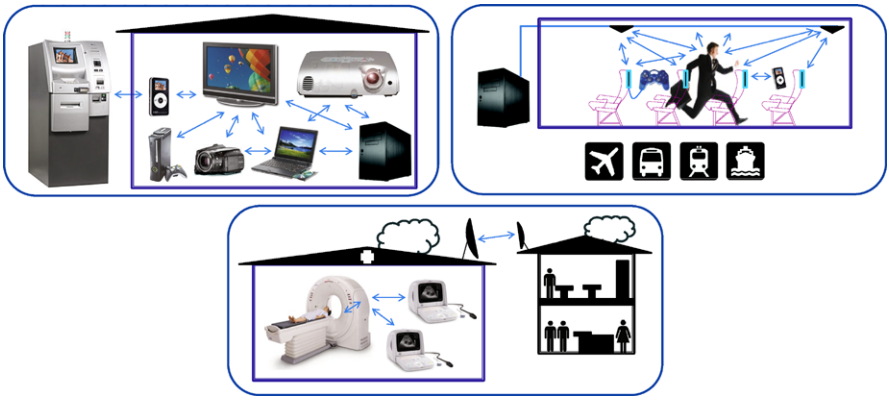

Fig. 2.14 Scenarios envisioned for mm-W/sub-mm-W: (*top-left*) kiosk, living room, office cubicle, and meeting room; (*top-right*) public transportation, and (*bottom*) medical and fix point-to-point links [GKZ+10] (©2010 IEEE, reproduced with permission)

channel at such Extra High Frequency (EHF) bands (30–300 GHz), mainly related with the confined propagation scenarios envisioned for Wireless Local Area Network (WLAN) and Wireless Personal Area Network (WPAN) [CTT+09]. Besides, some applications are included within the public transportation scenarios for multiple access, e.g., for In-Flight-Entertainment (IFE), see Fig. 2.14 (top-right), [Gar10, GKZ+10]. These environments differ from others due to the higher density of users, human behavior, and usual metal cabins. Indeed, mm-W/sub-mm-W radio channels (with wavelengths between 1 and 5 mm) do not follow the usual 2–5 GHz channel characteristics (e.g., see [YSH05] for 60 GHz channels), showing smaller delay spread [GKT+09], remarkable impact of shadowing due to the human activity [GKT+10a], important diffraction effects due to human bodies [JMK10, GKT+10a], high water vapor absorption, and different directional characteristics due to the high path-loss.

Thus, investigations about channel characteristics for different scenarios and antenna patterns, including directional and polarimetric information, are important issues for designing multi-Giga-bit/s access. Besides, new channel sounders, extensive measurement campaigns, analysis, and modeling will be required for proposing possible enhancement techniques, e.g., beamforming, macro-diversity, and seamless handover, among others.

The section is structured as follows. At first, the propagation phenomena are described to highlight the peculiarity of mm-W and sub-mm-W. Then, different channel sounder architectures and their characteristics are presented. At the end of the section, radio propagation channel analyses are summarized for different scenarios, namely: indoor, in-cabin, in-car, hospital, and outdoor.

2.1.5.1 Propagation Phenomena

To derive accurate deterministic mm-W and sub-mm-W channel models, the knowledge of the significant propagation mechanisms is very important. Propagation phe-

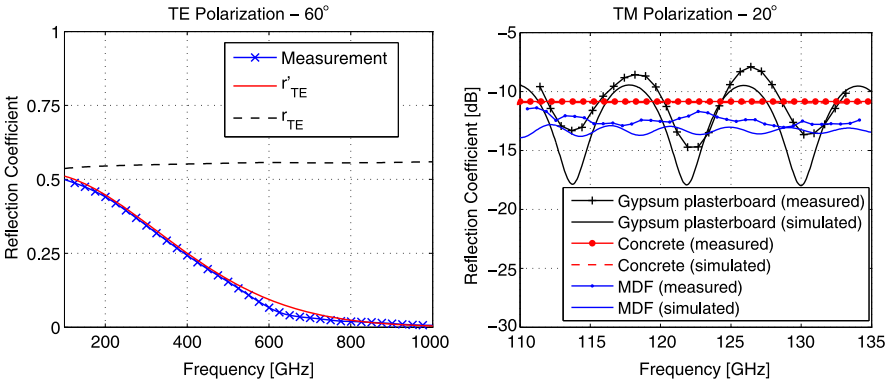

(a) Rough Surface. (b) Multiple Reflections.

Fig. 2.15 Calculated and measured reflection coefficient for a rough surface [PSKK07] and different optically thin materials [PSKK07]

nomena are significantly different than at lower frequencies due to the small wavelengths at 60 GHz and beyond 100 GHz. In the following, these phenomena and the possibilities to model them are presented. At first, scattering and reflection measurements are introduced, then the path loss at mm-W and sub-mm-W is analyzed, and at the end the effects of shadowing due to human activity are summarized.

The scattering from rough surfaces and the effect of multiple reflections have been investigated during the last years up to THz frequencies [PSKK07, PJKK08, JPJ+09]. In [PSKK07] the specular reflection from rough concrete plaster has been measured with terahertz time-domain spectroscopy. In this work the reflection coefficient r has been calculated from measurements of absorption coefficient and refractive index using the conventional Fresnel equations. Following Kirchhoff's Scattering theory [BS87], these coefficients need to be multiplied by the so-called Rayleigh factor, taking into account the surface roughness in order to obtain a modified reflection coefficient r'. A comparison between measurement and simulation results using this procedure is shown in Fig. 2.15(a) for frequencies between 100 GHz and 1 THz. The simulated reflection coefficient r fits with the measured data, but only for longer wavelengths. Except of these limited cases, the simulated conventional reflection coefficient deviates significantly from the measured one. The difference becomes more and more significant as the frequency increases. This is a consequence of the effective roughness of the material, which grows along with the scattering losses in the specular direction if the frequency increases. However, the modified reflection coefficient r' fits well with the measurement data in all the spectrum.

On the other hand, multiple reflections within materials significantly influence the radio wave propagation, especially in case of optically thin or layered materials. This propagation mechanism can be modeled by the so-called transfer matrix method [PJKK08]. Figure 2.15(b) shows measurement and simulation results for concrete, medium density fiberboard (MDF) and gypsum plasterboard samples. In

case of the concrete slab, a flat characteristic is observed. This behavior is due to the large thickness of the concrete slab compared to the wavelength of the propagated waves, and also due to the relatively high absorption losses of concrete. The reflection pattern of the MDF sample is similar to that of the concrete slab. However, it does differ in some details. The most significant difference is the influence of multiple reflections within the material, which can be clearly recognized as an oscillation in the frequency pattern. The multiple reflection effect is even more pronounced for the gypsum plasterboard sample, caused by the small absorption losses and the small sample thickness.

Other relevant propagation mechanism at 60 GHz and THz is the path-loss, especially if we consider that a likely application is the wireless interconnection of different electronic devices for ultrafast file transfer on a desktop or within indoor environments with TX-RX ranging from few centimeters to 10 m. In [JPJ+09] the path-loss for the desktop case has been characterized experimentally and compared to the two-ray model [HBH03] for frequencies between 290 and 310 GHz. Figure 2.16(a) illustrates the simulated distance dependent path-loss for 304.27 GHz. Besides, the two-ray model results and the free space loss are shown as reference. In addition, the same data are depicted for a frequency of 2.4 GHz, where current systems like Wi-Fi or Bluetooth are deployed. For 304.27 GHz, the combined direct and reflected rays cause alternating reinforcement and reduction of the signal power, with peak levels reaching up to 6 dB below free space loss. Regarding 2.4 GHz, the combined path-loss is always higher than free space loss (2–26 dB), whereas no fading dips can be observed. Figure 2.16(b) depicts the comparison between the two-ray model and measurements around the fading dip at 67.5 cm. The fitting between simulation and measurement shows that the two-path theory is well suited to describe the analyzed scenario. Moreover, Fig. 2.16(c) compares the empirical path-loss fitting obtained for different 60 GHz indoor environments, i.e., residential and hospital environments [KHS+10]. It was found that the empirical path-loss model for hospital environments fell between small rooms and residential Line-Of-Sight (LOS) environments, with path-loss exponents between 1.34 and 2.23 (for small rooms and residential between 1.53 and 2.44; shielded room 4.18). This is reasonable since the hospital environments have more metallic scattering objects than residential environments, but these environments are more spacious than a small room where wave scattering could be very rich.

Other relevant propagation phenomena at mm-W and beyond are the obstruction losses and the dynamics from LOS to Obstruction-LOS (O-LOS) due to the human activity, which is denoted by Garcia et al. as Shadowing By Human Bodies (SHB) [GKT+10a]. This is specially relevant for public transportation scenarios (see Fig. 2.14, top-right). More precisely, the Time-Varying Shadowing by Human Bodies (TVSHB) [GKT+10a] shows peculiar characteristics at mm-W compared to other frequencies (see Fig. 2.17). This is a consequence of the small Fresnel zones and, due to the body skin, reflects partially the waves, and the through body propagated waves are strongly attenuated. Therefore, short-term oscillations due to diffracting waves appear during the partial obstruction of the Fresnel zones (see Fig. 2.17, right and top-left). Besides, strong and long shadow fading events appear

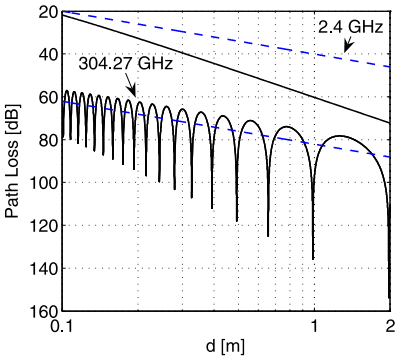

(a) Distance dependent path-loss, modelled by two-ray theory (solid line) and Friis' formula (dashed line).

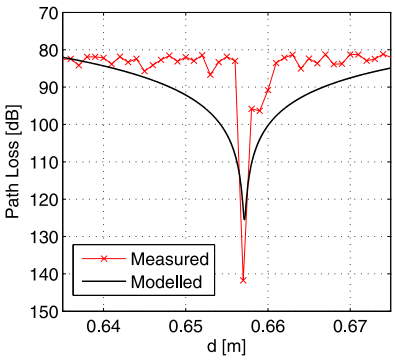

(b) Distance dependent path-loss, measured and simulated by two-ray theory (f=304.27 GHz).

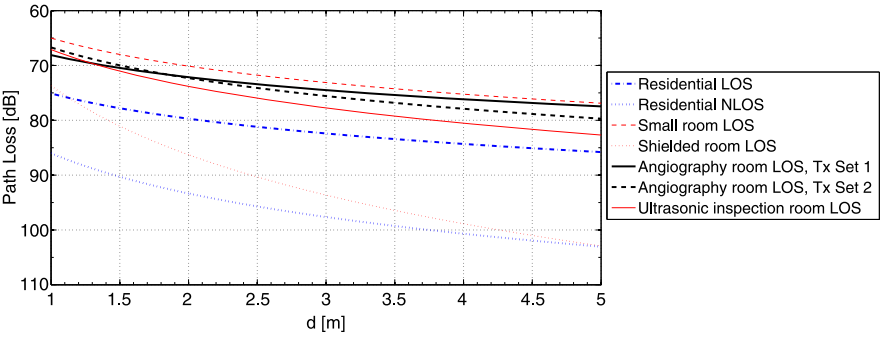

(c) Distance dependent path-loss, measured (fitting) for different indoor environments (f from 61 to 65 GHz).

Fig. 2.16 Measurement and simulation results of the path-loss for 60 GHz and THz applications [JPJ+09, KHS+10] (©2009 IEEE, reproduced with permission)

due to the total obstruction of the first Fresnel zone, including some contributions from reflected, diffracted, and wake through body propagated waves (more details can be found in [GKT+10a]).

Therefore, the main challenge for the statistical characterization of TVSHB is the real-time measurement (wideband) of the duration/depth of each obstruction event. For instances, for the isolation of the events in Fig. 2.17, right, the relative receiver power and its gradient were classified using thresholds of -2 dB and ± 0.3 dB/100 ms, respectively (see also Fig. 2.17, bottom left). From preliminary results within an Airbus-340 cabin [GKT+10a], the analyzed TVSHB events indicated fading dynamics up to about ± 10 dB/100 ms, with maximum depth durations of 8 s. These are relevant channel characteristics for a proper link budget and MAC simulations in 60 GHz WLAN/WPAN.

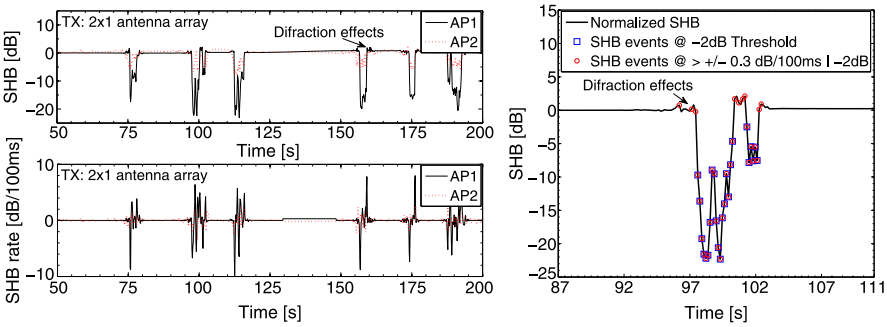

Fig. 2.17 TVSHB characteristics during obstruction LOS using 2 × 1 antenna arrays for two distributed access points (AP): (*top-left*) SHB, (*bottom-left*) SHB rate, (*right*) SHB around isolated human events [GKT+10a] (©2010 EurAAP, reproduced with permission)

2.1.5.2 Channel Sounding

Channel sounding at mm-W/sub-mm-W is a challenging task, and nowadays real-time implementations have been realized at mm-W. Some sounders based on VNA and real-time hardware have been introduced in different publications, e.g., see [GKT+09, JK09, FS10, GWF+10, KSH+10, Kiv07, ZBN05]. One of these solutions, developed by MEDAV GmbH and TU-Ilmenau, fulfill both MIMO and UWB characteristics in real-time [GKT+09]. This sounder is based on a commercial UWB channel sounder and 60 GHz up/down-converters as described in Fig. 2.18 for a Single-Input Single-Output (SISO) case. This solution is based on M-Sequence UWB radar chip-sets for baseband (0 to 3.5 GHz), and two stages of frequency conversion from/to the UWB band (3.5 to 10.5 GHz) and to/from the 60 GHz band (59.5 to 66.5 GHz). The reference LO is a 7-GHz signal which is distributed within the system including different multiplication stages. Distributed MIMO capability is supported at the UWB stage with multiple modules. This modular concept allows one to replace the 60-GHz stage for different single and dual-polarized frontends. Note that the system has a common chain for obtaining I and Q signals at baseband. Thus, for calibration purposes, a serial I/Q concept was implemented based on a 90° LO phase sifting and a switch between 0° and 90° LO at the receiver chain. During I/Q and frequency response calibrations (using a high-precision step attenuator and a delay line at the UWB stage), the PC-based system saves the calibration vectors, which can be used in postprocessing for data analysis. Back-to-back calibration at 60 GHz (including a high-precision attenuator) and cross-talk calibration (at UWB with 50 Ohm terminations) are performed for this channel sounder architecture.

The performance of this sounder is presented in Fig. 2.19, based on a 3-GHz bandwidth implementation at 60 GHz, with real-time Single-Input Multiple-Output (SIMO) capability (1 TX and 2 RX), and linear polarization. The frequency/phase responses and impulse response from back-to-back measurements using a high-precision coaxial attenuator (59 dB) after calibrations for both TX-RX pairs (CH1 and CH2) are presented. Once the calibration was performed and the frequency

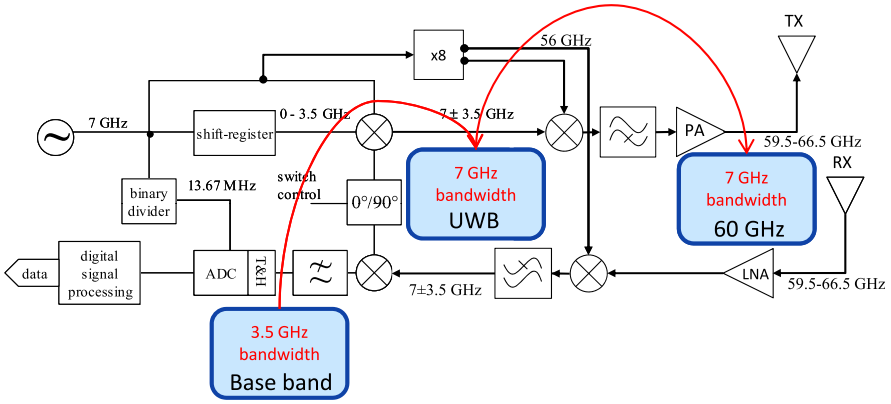

Fig. 2.18 60-GHz-UWB real-time channel sounder architecture [GKZ+10] (©2010 IEEE, reproduced with permission)

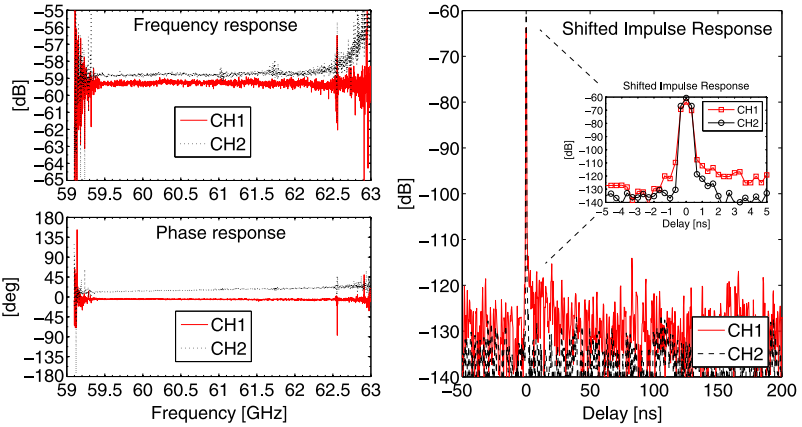

Fig. 2.19 60-GHz real-time channel sounder performance [GKZ+10] (©2010 IEEE, reproduced with permission)

span set (in postprocessing from 59.5 to 62.5 GHz), the dynamic range of the system reaches up to approximately 50 dB, with maximum detectable paths at ∼ 585 ns and a resolution better than 1 ns. These characteristics guarantee sufficient dynamic range for TVSHB analysis and present the highest sounding resolution reported in literature based on a real-time SIMO configuration. This configuration is also useful for macro-diversity analysis at mm-W. Measurements campaigns based on this channel sounder have been reported in [Gar10, GKT+10a, GKZ+10, GKBT09]. Examples of measured Power Delay Profile (PDP) (TX-RX in alignment), and both RMS delay spread and coherence bandwidth (at 0.9 correlation) under TVSHB (dynamics) are presented in Fig. 2.20.

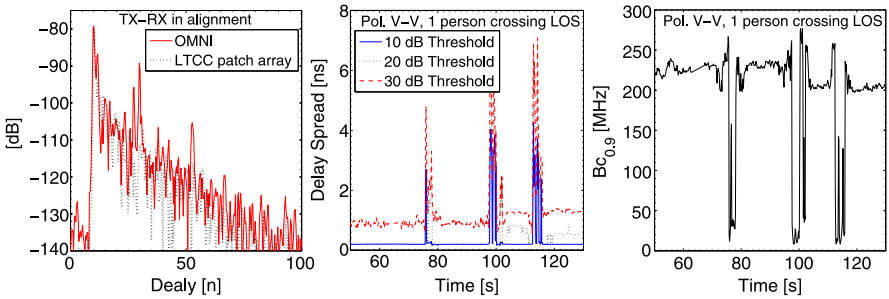

Fig. 2.20 60-GHz real-time channel results: (*left*) PDPs with two different antennas within the Airbus-340, (*center*) RMS delay spread under TVSHB, and (*right*) coherence bandwidth, Bc, at 0.9 correlation under TVSHB [GKBT09]

Another real-time sounder implementation, based on Frequency Modulated Continuous Wave (FMCW) techniques, has been presented in [FS10], and some channel results in [GWF+10]. In this case, the channel is repeatedly excited with a Continuous Wave (CW) signal (chirp) that is swept across the channel in the frequency range from 59 GHz to 67.5 GHz. Besides, this sounder allows frequency scaling for the final bandwidth at 60 GHz up to 300 MHz $\times$ 4 for the results presented in [GWF+10]. The phase noise for this sounder was predicted to be about -45 dBc, the dynamic range about 40 dB (at 260 MHz sweep), and the Doppler/delay profile demonstrated a small degradation [FS10].

On the other hand, channel sounders using VNAs and up/down-converters, e.g., [JK09] and [KSH+10], have been implemented with the advantage of high dynamic range and huge bandwidth. The drawbacks of these solutions are the time consumption for performing measurements and the feasibility of real-time measurements only when using single tones. These channel sounders are useful for office and home environments as described in Fig. 2.14 (top-left), where channels are mainly LOS with very long coherence.

Finally, it is worth mentioning that the performance analysis of new enhancement techniques for 60 GHz WLAN/WPAN, for instance, pixel-partitioning and multiantenna-beam methods [SOK+08, PGR09], require real-time sounding at 7 to 9 GHz bandwidth. Besides, multiantenna and dual-polarization capabilities (the first 60 GHz dual-polarized architecture with phase adjustment was presented in [GM+10]) are also required to investigate macro-diversity, seamless handover, beamforming, and polarization mismatch. Moreover, PHY channelization is important for channel sounding at mm-W to cover most of the 60 GHz spectrum for analyzing Signal-to-Noise Ratio (SNR) and frequency reuse of different subbands [GKZ+10, GM+10].

2.1.5.3 Channel Analysis for Different Scenarios

Besides the pure characterization of the radio propagation channel, channel measurements are used to build statistical channel models. In [CAS08] a new approach

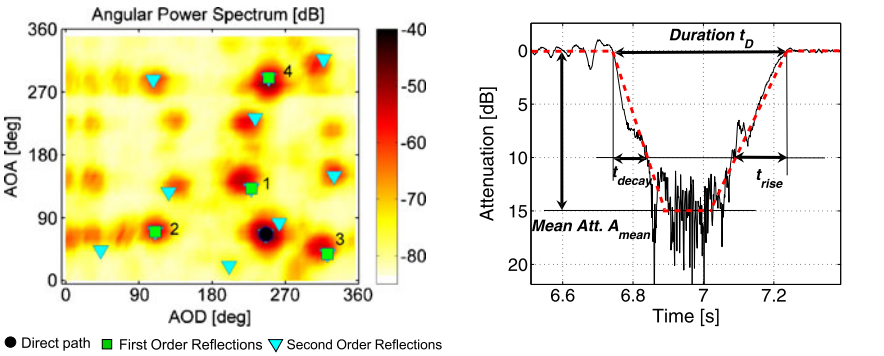

(a) Measured angular power spectrum and AoA/AoD predicted by ray-tracing [KJ09] (©2009 IEEE, reproduced with permission).

(b) Example for temporal characteristics of human induced shadowing events with parameter definitions [JMK10] (©2010 IEEE, reproduced with permission).

Fig. 2.21 Double directional channel measurement results and example for temporal characteristics of human induced shadowing events

based on α-stable distributions is proposed as an alternative to the widely used Saleh–Valenzuela model [SV87]. The model is based on a thorough study of the second-order statistical properties of the indoor channel in the 60-GHz band based on 2-GHz bandwidth measurements. In order to show that the model is appropriate, observed impulse responses have been tested against model results. Besides, the visible closeness between simulated and real data has indicated that the model is able to detect the time of arrival of multipath components with a great precision. In addition to the comparison between single impulse responses, the cumulative distribution functions of RMS delay spread from observed impulse responses and those generated by the model have shown a good fit.

On the other hand, the knowledge of angular dispersive channel characteristics is important for modeling, when beam steering [IEE09, IEE10] should be applied. In [KJ09, JK09], double directional mm-W channel measurements and channel characteristics derived by ray tracing in a fully furnished conference room have been compared (see Fig. 2.21a). In this figure the measured angular power spectrum depending on AoA and AoD is shown and compared to ray tracing results. For first- and second-order reflections, the corresponding paths, derived by ray tracing, have been identified and have shown a good agreement with the measurement data. Although material parameters have been used from literature instead of performing a site-specific calibration, the path-loss predicted for the different rays is in reasonable agreement with the measurements (mean error of 0 dB and a standard deviation of 4 dB). Another directional channel analysis has been performed in a conference room [GTWH10], where the Space-Alternating Generalized Expectation-maximization (SAGE) algorithm has been used. This work concluded that in LOS scenarios the strongest component contributes to 95% of the available power, and the strongest component in Non-Line-Of-Sight (NLOS) scenarios is on

the order of 20 dB lower than the LOS component. Besides, the authors concluded that none of the channels can be regarded as having rich scattering.

Another important issue is the time variability of the channel in environments with stationary devices. The nonstationarity of the 60-GHz channel mainly appears from moving people that may attenuate the communication link by 20 dB and more [CZZ04, GKT+10a, JMK10]. Figure 2.21(b) shows an exemplary human-induced shadowing event obtained from experimental measurements (solid line) as well as the shape of a model (dashed line) proposed by Jacob et al. to describe this event [JMK10]. Four parameters have been chosen to describe a shadow fading event: the duration t_D, the decay time t_{decay}, the rising time t_{rise}, and the mean attenuation A_{mean} calculated in the interval $\frac{1}{3}t_D < t < \frac{2}{3}t_D$. The above-mentioned parameters have been statistically analyzed based on several hundreds of measurements. During the measurements, the received power of the LOS path was observed while a person was moving around within a living room scenario. The investigations have shown that the drop of signal level happens in the order of tens of milliseconds. On average the signal decreases by 20 dB in 230 ms, whereas it takes 61 ms for a reduction of 5 dB. In 90% of the cases, the signal decrease took at least 4 ms for a 1 dB, 27 ms for a 5 dB, and 101 ms for a 20 dB threshold. The duration of a single fading event reach up to 550 ms on average, and the mean attenuation A_{mean} ranges between 6 and 18 dB, whereas the maximum attenuation can reach up to 36 dB. These parameters can be statistically modeled by well-known distributions and serve as guidelines for 60 GHz WLAN MAC layer development.

For aircraft cabin applications [Gar10, GKT+09, GKBT09, GKT+10a, GKZ+10], redundancy (macro-diversity or handover) must be addressed as a possible system enhancement against the channel dynamics, mainly due to the high SHB[2] margins for network planning. In [GKT+09, GKT+10a, GKZ+10], two measurement campaigns were performed within an Airbus-340 cabin, taking into account different redundant cell configurations (distributed Access Point (AP); AP1 and AP2), human activities, and TX antennas (horns, open-waveguides, and cavity/patch arrays). The TVSHB when passengers were walking, blocking, and standing up has been considered for the analysis of shadow fading in dB (denoted by SHB in Fig. 2.22, left), fading-rate in dB/ms (denoted by SHB rate in Fig. 2.22, center), depth-duration, SHB auto-correlation, and cross-correlation between APs. The TVSHB events showed up to about ±10 dB/100 ms of fading-rate, with maximum depth durations of ∼8 s, median depth durations of ∼0.5 s, shadow fading up to ∼–20 dB at 10% outage, and stationary intervals between 112 ms and 1 s (see also Fig. 2.23).

These SHB results need to be considered for in-cabin coverage analysis. For instance, Fig. 2.22 (right) shows the SNR outage results plotted for different antennas (horn and open waveguide), taking into account an Airbus-340 cabin in static conditions [GKZ+10]. Here, 50% of the in-cabin coverage area fulfill the SNR requirements for compressed video, but if SHB is considered, redundancy must be addressed.

[2]SHB refers to the normalized receiver power with respect to LOS conditions during each human event.

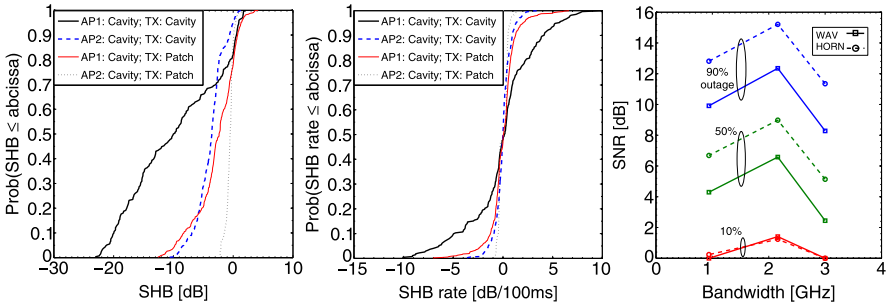

Fig. 2.22 Examples of the CDFs of SHB [GKT+10a] (©2010 EurAAP, reproduced with permission) (*left*), CDFs of SHB rate (*center*), and SNR coverage (*right*) for the Airbus-340 in-cabin channel at mm-W [GKZ+10] (©2010 IEEE, reproduced with permission)

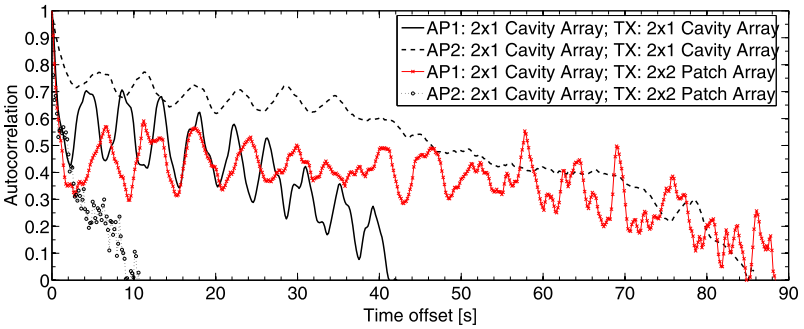

Fig. 2.23 Real-time autocorrelation of the SHB for the in-cabin channel at mm-W for a 1×2 AP configuration and different antennas [GKT+10a] (©2010 EurAAP, reproduced with permission)

Other analyses claim that the best configuration against TVSHB is obtained combining wide and narrow beam patterns at TX and RX, respectively [GKT+10a]. This can reduce both the shadowing margins at 10% outage and the fading depths during each event. Moreover, based on another TVSHB characterization described in [GKT+09], SHB margins can be reduced by 5 dB (mean) using wider beam patterns, obtaining more than 50% relative power increments for link budgets. For the same configurations, the SHB rate can be improved up to ± 3 dB/100 ms at 99% reliability.

Results from dynamic mm-W channel measurements and modeling in a shielded room and hospital environments were presented in [KSH+10] and [KHS+10]. The goals of these works were to investigate potential and feasibility of 60-GHz radios for multi-Giga-bit/s short-range communications in indoor medical applications. The results revealed that shadowing by human activity can reach up to 10 dB (for fixed TX/RX positions). With a small movement of 20 cm, the normalized received power has changed by as much as 6 dB. Besides, for indoor propagation modeling purposes, the empirical path-loss exponent for a shielded room was estimated close to 4, and for other environments, between 1.54 and 2.23.

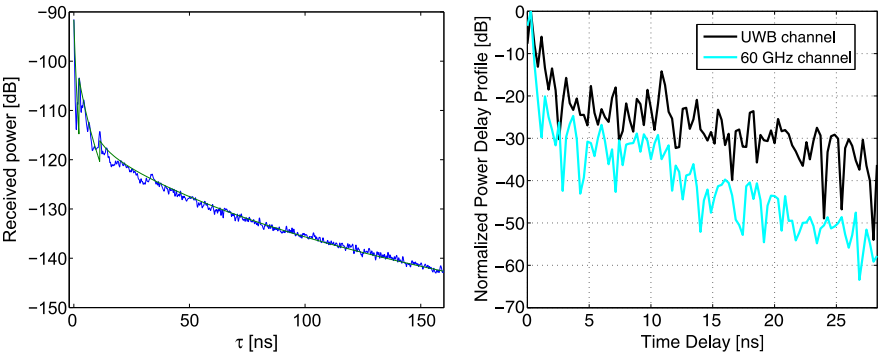

(a) Example of measured PDP and its fitting using the power law model for the shielded room environment [KSH+10] (©2010 IEEE, reproduced with permission).

(b) Normalized PDPs for a 60 GHz and a UWB in-car-channel [SJK10](©2010 EurAAP, reproduced with permission).

Fig. 2.24 Power delay profile for a shielded room environment [KSH+10] and an in-car environment [SJK10]

The main difference between propagation in a shielded room and other indoor environments considered in this section is the occurrence of clustering in the PDPs (see, e.g., Fig. 2.24a and Fig. 2.20, left). In the investigated shielded room, the PDPs consisted of 3 clusters in many cases. It turned out that the PDPs were better modeled by the power law of the paths, rather than conventional exponential decay. Additionally, a strong correlation between model parameters, e.g., between peak power and power decay [KSH+10], was observed.

The RMS delay spread was estimated for all indoor environments to be lower than 15 ns for thresholds of 10, 20, and 30 dB (see, e.g., Fig. 2.20, center).

The 60-GHz band is also of interest for applications where distances of less than 1 or 2 meters have to be linked, like the in-car scenario. In order to save installation costs, particularly in luxury class cars which are equipped with infotainment and entertainment devices, replacing wired by wireless communication is of great interest. Figure 2.24(b) shows the normalized PDPs for a 60-GHz and a UWB in-car channel [SJK10]. The transmitting antenna has been installed below the interior rear view mirror. The receiver was placed on the height of the rear seat armrests, assuming passengers accessing the car network with their own handheld devices. Both PDPs exhibit a very strong direct path, which reflects the LOS situation of this Rx position. It appears that the power decay time constant of the multipath components for the 60-GHz channel is in general much higher than for the UWB channel. The possible explanation is that the multipath components of the 60-GHz frequency band are strongly attenuated by the leather-cladding of the doors and seats in contrast to the UWB frequency band where a reflection at the metallic structure is possible. Other investigations lead to the conclusion that the antenna alignment, particularly when the main lobe of the antenna pattern is wide enough, does not play a significant role for UWB and 60-GHz system performance. Furthermore, a feasibility study which was based on the conducted measurements has shown that both systems can be re-

alized even in such a multipath-rich environment. In these scenarios, inter-symbol interference becomes a limiting factor at increased rates.

Finally, the mm-W band is also of interest for long range outdoor point-to-point links. An example about channel investigations for this kind of links is addressed in [GKKV10]. The authors have found that the LOS path is up to about 30 dB stronger than other MPCs. This is caused by the high directivity of the parabolic antennas (45 dBi gain) used during the measurement campaigns. Therefore, in E-band point-to-point channels, the plane waves propagate like in free space. For link budgets including large-scale channel fading, the authors have proposed to introduce a fading margin of 2 dB considering both the high channel bandwidth and the focus ability of high-gain antennas. Besides, a model of rain attenuation for E-band at 80 GHz is proposed in this work based on rain attenuation models from ITU-R [IR03]. Based on the proposed model, rain attenuations were estimated to be about 8.7 dB/km and 19 dB/km, for medium and downpour rainfalls, respectively.

2.2 Channel Parameter Estimation

2.2.1 High-Resolution Parameter Estimation

High-resolution parameter estimation is an important processing step for many propagation (channel sounding) measurements. The main objective of the procedure is to provide a description of the radio propagation channel that is—with certain limitations—independent of the employed measurement equipment. The obtained model parameters can be later used, for example, to (i) simulate a MIMO radio link with an arbitrary array configuration and other system parameters or (ii) derive parameters for stochastic channel models, such as cluster-based models.

This section describes the current state-of-the-art in high-resolution parameter estimation, reflecting the latest developments in the COST 2100 framework. First, the underlying modeling assumptions and their alternatives are summarized. Then, brief descriptions of available algorithms are given. Finally, the clustering of the resulting propagation path parameters is discussed.

2.2.1.1 On the Model Assumptions and Initialization

Let us have a sampled realization of the multidimensional radio channel $\mathcal{H} \in \mathbb{C}^{M_f \times M_t \times M_r}$ with M_f frequency points, M_t transmit antennas, and M_r receive antennas. In the following, a vector form $\mathbf{h} = \mathrm{vec}(\mathcal{H}) \in \mathbb{C}^{M \times 1}$ with $M = M_f M_t M_r$ is used for clarity. High-resolution parameter estimation methods are based on modeling the channel as a superposition of P Multi-Path Components (MPCs) as

$$\mathbf{h}_S = \sum_{p=1}^{P} \mathbf{h}_s(\Theta_p), \tag{2.2}$$

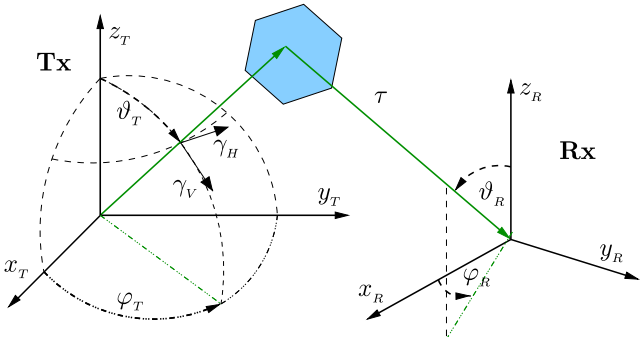

Fig. 2.25 Illustration of the double-directional propagation path parameters [Sal09]

where $\mathbf{h}_s(\Theta_p)$ denotes the contribution of the pth specular-like (hence subscript s) propagation path. Typically, the MPCs are modeled as planar wavefronts at both link ends. Also, the narrowband assumption of the propagation channel is commonly made, i.e., the complex response of the antennas, along with the interactions that the radio waves undergo, are assumed to be constant over the frequency band occupied by the employed RF signal. Hence, a single path is parameterized by

$$\Theta_p = \left[\tau^{(p)} \phi_t^{(p)} \theta_t^{(p)} \phi_r^{(p)} \theta_r^{(p)} \gamma_{HH}^{(p)} \gamma_{HV}^{(p)} \gamma_{VH}^{(p)} \gamma_{VV}^{(p)}\right]^T, \tag{2.3}$$

where τ denotes the Time Delay of Arrival (TDoA), $\phi_{r/t}$ and $\theta_{r/t}$ denote the azimuth and elevation angles at Rx/Tx, respectively, and $\gamma_{ij}^{(p)}$ denote the complex path weights of each $ij \in \{HH, HV, VH, VV\}$ polarization component. The propagation path parameters are illustrated in Fig. 2.25.

The contribution of a single Multi-Path Component (MPC) in the observed radio channel, including the antennas, is given by

$$\mathbf{h}_s(\Theta_p) = \sum_i \sum_j \mathbf{b}_{r,j}\left(\phi_r^{(p)}, \theta_r^{(p)}\right) \otimes \mathbf{b}_{t,i}\left(\phi_t^{(p)}, \theta_t^{(p)}\right) \otimes \mathbf{b}_f\left(\tau^{(p)}\right) \cdot \gamma_{ij}^{(p)}. \tag{2.4}$$

The vectors $\mathbf{b}_{r,j/t,i}(\phi_{r/t}^{(p)}, \theta_{r/t}^{(p)}) \in \mathbb{C}^{M_r/M_t \times 1}$ denote the angle-dependent responses (narrowband steering vectors) of the receive or transmit (r/t) antenna arrays for the horizontal $(i/j = H)$ or vertical $(i/j = V)$ polarization, and $\mathbf{b}_f(\tau^{(p)}) \in \mathbb{C}^{M_f \times 1}$ is the frequency response resulting from the delay of arrival $\tau^{(p)}$.

The propagation path model (2.2) has the ability to separate the influence of the antenna array response, as the parameters in (2.3) depend only on the propagation channel itself. Hence, it is a very intriguing approach to try to model the complete measured propagation channel as a superposition of propagation paths along with the assumption of i.i.d. complex white normal distributed measurement noise $\mathbf{n}_w \sim \mathcal{CN}(\mathbf{0}, \sigma_n^2 \mathbf{I})$ as

$$\tilde{\mathbf{h}} = \mathbf{h}_S + \mathbf{n}_w. \tag{2.5}$$

This model can be reasonably accurate especially in outdoor scenarios. This was indicated, e.g., in [EWLT10], where the goodness of fit was compared in terms of both

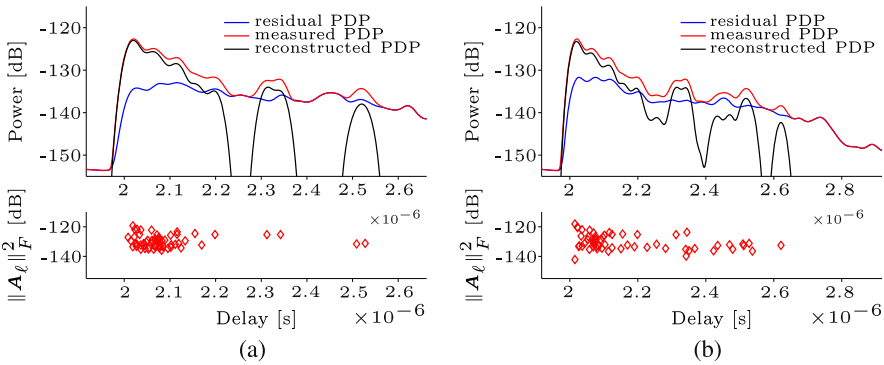

Fig. 2.26 Measured, reconstructed, and residual PDP using (**a**) SIC-based, and (**b**) ADPP-based initialization [SCPF09]

power and capacity from measurements at 285 MHz. However, it has been shown that this approach comes with several deficiencies including (i) a huge number of MPCs is required to obtain a decent fit to a given channel realization [SCPF09, MRAB05], (ii) depending on the initialization technique, the path estimates may be concentrated only on the early, high-power part of the delay profile [SCPF09], and (iii) inference based on describing the channel with propagation paths only (2.5) may result in false conclusions on the performance measures such as channel capacity [RSK06].

In [SCPF09], the authors propose an alternative approach for initializing high-resolution propagation path estimation algorithms with the aim of extracting channel features over the whole delay range of the channel response. The late arriving parts have low power but still contain information which may be useful for, e.g., localization purposes. The contribution [SCPF09] considers the extraction of such features by designing initialization steps which do not only consider the minimization of the residual power. Instead of using conventional Successive Interference Cancellation (SIC) methods for detecting paths from the residual signal based on the L_2-norm, the algorithms are initialized by either (i) dividing the effective delay range into a number of equidistant bins and using a fixed number of starting values for path estimates within each bin or (ii) detecting the maxima in the PDP or Azimuth-Delay Power Profile (ADPP) and assigning a number of initial path estimates for each of such maxima. A simple measure such as the widely used ratio of the residual power versus the measured power is inadequate to evaluate the channel estimates. As can be seen in Fig. 2.26, the lower residual power in the early part of the channel response would lead with this measure to the conclusion that the SIC-based method provides better channel parameter estimates. However, it neglects the MPCs in the later part of the channel response almost completely. The proposed approaches of [SCPF09] provide path estimates for a wider delay range, yielding a more realistic estimate of the overall radio channel. Figure 2.26 shows an estimation example comparing SIC and ADPP-based initialization.

While leading to a better extraction of path parameters in the late part of the response, the estimation method suggested in [SCPF09] is not concerned with catching *all* the power in the full response. Thus a significant portion of the power in the channel remains unaccounted for, see the residual PDPs in Fig. 2.26. Another approach introduces a so-called Dense Multipath Component (DMC) as a stochastic part $\mathbf{h}_D \sim \mathcal{CN}(\mathbf{0}, \mathbf{R}_D)$ in the channel model [Ric05, Sal09], yielding

$$\mathbf{h} = \mathbf{h}_S + \mathbf{h}_D + \mathbf{n}_w. \tag{2.6}$$

The DMC describes the contribution in the radio channel from diffuse scattering, which is difficult and computationally exhausting to capture using a superposition of deterministic propagation paths (2.2) only. From the point of view of high-resolution propagation path parameter estimation, the model (2.6) can be simplified as

$$\mathbf{h} = \mathbf{h}_S + \mathbf{n}_D, \tag{2.7}$$

where $\mathbf{n}_D = \mathbf{h}_D + \mathbf{n}_w \sim \mathcal{CN}(\mathbf{0}, \mathbf{R}_D + \sigma_n^2 \mathbf{I})$. Furthermore, [Ric05, Sal09] suggest the use of a Kronecker model to describe the DMC covariance matrix as $\mathbf{R}_D = \mathbf{R}_R \otimes \mathbf{R}_T \otimes \mathbf{R}_f$. The Kronecker model provides computational benefits and limits the number of free parameters, which results in good identifiability of the model. However, due to the presence of paths $\mathbf{h}_S$ (2.2), the overall channel (2.7) is not a Kronecker model.

To conclude, the benefits of having the DMC in the channel model (2.7) include: (i) the detection of significant propagation paths over the whole parameter range of interest is improved, (ii) a better fit of the overall channel is obtained, and (iii) computational complexity of the resulting parameter estimator is reasonable. A downside of the currently employed DMC models is that they do not directly support the separation (deembedding) of the radio propagation channel from the antenna arrays. However, active research to overcome such limitations is currently taking place, see [KLT09, SPH+10, QOHDD10]. For more discussion on DMC, see Sect. 3.3.

In [SSM10], the MPC model (2.4) was extended to a frequency-dependent, wideband antenna array model. A wideband antenna array model is necessary if the frequency response of the antennas varies over the signal band, or if the array size becomes significant.[3] The frequency dependence of the wideband antenna array model invalidates the Kronecker separability of (2.4). However, one of the benefits of the wideband modeling is that the commonly assumed $\lambda/2$ restriction on the antenna spacing may be relaxed. This is illustrated in Fig. 2.27 for a 10-element Uniform Linear Arrays (ULA) with 5-cm antenna spacing. The ambiguity function (correlation of the antenna array response at different angles) is defined as

$$C(\phi_i, \phi_j) = \frac{\operatorname{vec}(\mathbf{B}_r(\phi_i))^H \operatorname{vec}(\mathbf{B}_r(\phi_j))}{\|\operatorname{vec}(\mathbf{B}_r(\phi_i))\|_F \|\operatorname{vec}(\mathbf{B}_r(\phi_j))\|_F}, \tag{2.8}$$

where $\mathbf{B}_r(\phi_i) \in \mathbb{C}^{M_r \times M_f}$ denotes the wideband "steering matrix." The wideband model does not suffer from the angular ambiguity present at the highest frequency

[3] The antenna array size can be considered insignificant while $D \ll c/B$, where D is the diameter of the smallest sphere enclosing the array, c is the speed of light and B is the signal bandwidth.

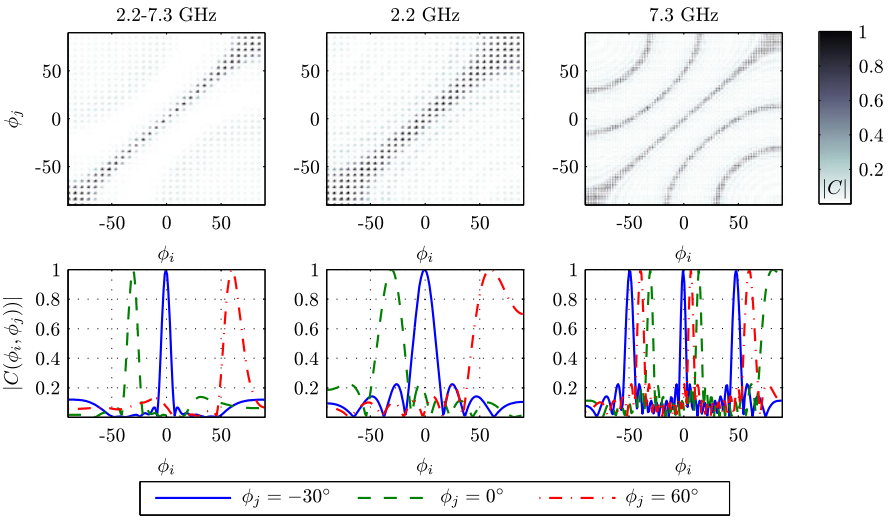

Fig. 2.27 Ambiguity function of a (ULA-10, 5 cm antenna separation) for UWB (2.2–7.3 GHz) antenna array model compared to narrowband model at 2.2 GHZ ($\lambda_l \approx 13.6$ cm) and 7.3 GHz ($\lambda_h \approx 4.1$ cm) [SSM10] (©2010 IEEE, reproduced with permission)

and has also improved resolution (narrower mainlobe) than at the lowest frequency [SSM10].

2.2.1.2 Algorithms

The notion of high-resolution parameter estimation implies the ability of an algorithm to distinguish between multiple closely separated and/or correlated propagation paths. Figure 2.28 provides a classification of available parameter estimation techniques. The methods that are currently widely used and can be classified as high-resolution techniques include subspace-based techniques such as Estimation Of Signal Parameters via Rotational Invariance Techniques (ESPRIT) [PRK85] and its variations [HZMN95], RAnk Reduction Estimator (RARE) [PMB04], Maximum Likelihood (ML)-based methods including SAGE [FTH+99] and Iterative Gradient-Based ML Parameter Estimation Algorithm (RIMAX) [Ric05], as well as sequential estimation (Bayesian filtering) based Extended Kalman Filter (EKF) [SRK09] and particle filter [YSK+08]. Recent summaries of the available high-resolution parameter estimation techniques can be found in [Yin06, Sal09].

The subspace-based methods rely on the model (2.5), with the additional assumption of $\mathbf{h}_s(\Theta_p) \sim \mathcal{CN}(\mathbf{0}, \mathbf{R}_S)$. The eigenvalue decomposition of the data covariance matrix is then given by

$$\tilde{\mathbf{R}} = \mathcal{E}\{\tilde{\mathbf{h}}\tilde{\mathbf{h}}^H\} = \mathbf{U}\boldsymbol{\Lambda}\mathbf{U}^H = \mathbf{U}_s\boldsymbol{\Lambda}_s\mathbf{U}_s^H + \mathbf{U}_w\boldsymbol{\Lambda}_w\mathbf{U}_w^H, \tag{2.9}$$

where $\mathbf{U}_s \in \mathbb{C}^{\tilde{M}\times P}$ and $\boldsymbol{\Lambda}_s \in \mathbb{R}^{P\times P}$ denote the eigenvectors and eigenvalues associated with the signal subspace with P sources, whereas $\mathbf{U}_w \in \mathbb{C}^{\tilde{M}\times(\tilde{M}-P)}$ and

Static Model		Dynamic Model
Spectral-based	Maximum likelihood	Kalman filters
- Beamforming (Bartlett, MVDR)	Stochastic ML	- Extended Kalman filter (EKF)
Subspace-based	Deterministic ML	- Unscented Kalman filter (UKF)
- MUSIC (spectral)	- SAGE	Sequential Monte Carlo
- ESPRIT, RARE (parametric)	- RIMAX	- Particle filter

Fig. 2.28 Classification of parameter estimation techniques [Sal09]

$\boldsymbol{\Lambda}_w \in \mathbb{R}^{(\tilde{M}-P)\times(\tilde{M}-P)}$ denote those of the noise subspace, which is orthogonal to the signal subspace. The symbol $\tilde{M} \leq M$ denotes the length of vector $\tilde{\mathbf{h}}$, which may be only a subset of the complete data model. A limitation of the subspace-based techniques is the fact that they require a sufficient number of realizations to obtain reliable estimates of the subspaces. ESPRIT is further applicable only to array geometries, where the array may be divided into a number of equidistantly spaced and identical subarrays.

The multidimensional Unitary ESPRIT algorithm was recently applied in [KH08, KdJBH08] for nonstationary SIMO measurements. The measurement setup employed a 31-element tilted cross array with three 11-element subarrays. An estimate $\hat{\tilde{\mathbf{R}}}$ of (2.9) was obtained from 10 consecutive snapshots. This allowed one to identify a maximum of 10 Direction of Arrival (DoA) estimates for each delay bin. In other words, the delay estimates $\hat{\tau}$ were in fact not high-resolution, as they were based on the Channel Impulse Response (CIR) delay bins.

Other contributions in subspace-based high-resolution parameter estimation methods include [GR07b], where a Root-MUSIC-based 2-D estimation algorithm was proposed for cylindrical antenna array configuration, as well as [GR07a], where RARE [PMB04] was employed for DoA estimation.

The ML-based methods, i.e., SAGE and RIMAX are perhaps currently the most commonly applied methods for high-resolution propagation parameter estimation. They are based on optimizing the initial parameter estimates, typically obtained by a SIC-based global grid search procedure, by assuming either the data model (2.7) or (2.5), and the probability density $\mathbf{h} \sim \mathcal{CN}(\mathbf{h}_S(\boldsymbol{\Theta}), \mathbf{R})$. The parameter estimates are found by maximizing the corresponding likelihood function

$$p(\mathbf{h}|\boldsymbol{\Theta}, \mathbf{R}) = \frac{1}{\pi^M \det(\mathbf{R})} e^{-(\mathbf{h}-\mathbf{h}_S(\boldsymbol{\Theta}))^H \mathbf{R}^{-1} (\mathbf{h}-\mathbf{h}_S(\boldsymbol{\Theta}))}. \tag{2.10}$$

Both SAGE and RIMAX are iterative procedures for finding the optimal parameters. In SAGE, the likelihood function (2.10) is maximized w.r.t. a subset of (or even a single) parameters at a time, keeping the rest of the parameters fixed. Each complementary subset is optimized in alternating fashion until convergence is reached. The beauty of SAGE is that the computational complexity of a single update can be controlled by the choice of the size of the parameter subset. On the other hand, a poor choice of subsets may reduce the convergence speed. RIMAX relies on a gradient-based optimization algorithm, which typically leads to faster convergence.

The parameters may be updated jointly or in subsets to reduce computational complexity. However, the parameter subsets, e.g., groups of paths, should be arranged so that correlated MPCs are optimized jointly. Also the introduction of the DMC (2.7) to support the high-resolution estimation of propagation path parameters was originally proposed for RIMAX [Ric05]. Both SAGE and RIMAX have been widely used within the COST 2100 framework, see, e.g., [CTW+07, SCPF09, KST08, ZTE+10, NKJ+10, BDHZ10, EWLT10].

A parametric study comparing the DoA estimation performance of beamforming, MUltiple SIgnal Classification (MUSIC), ESPRIT, and SAGE was conducted in [SGL07]. Simulations using multiple paths with different power levels resulted in the conclusion that SAGE outperforms the other compared methods, especially in terms of estimation accuracy for the paths other than the strongest one. In [GTS+10], an attempt was made to compare the performance of ESPRIT and RIMAX in estimating the MPC parameters in the presence of DMC. Although RIMAX clearly outperforms ESPRIT as expected, it is also evident that there would be much room for improvement in terms of correct pairing of the simulated parameters with the estimated ones.

The contribution [SKI+10a] proposes an approach, where initial MPC estimates are found using SAGE, after which they are clustered. The MPCs of each cluster are then refined using an extension of the subspace-based Method Of Direction Estimation (MODE) [SS90] algorithm. The approach in [SKI+10a] is motivated by the degraded performance of SAGE while estimating coherent signals.

The algorithms presented so far assume that the propagation path parameters remain constant during the observation period and are more or less independent from an observation to another. However, as channel sounding measurements are often performed in a dynamic, mobile environment, a state-space model along with a sequential estimation technique may be employed. Two such Bayesian filtering approaches have been proposed recently, one relying on the EKF [SRK09] and another utilizing the particle filter [YSK+08]. In both methods, the propagation path parameters $\boldsymbol{\Theta}$ (2.3), as well as their rate of change $\Delta\boldsymbol{\Theta}$, are modeled as the state $\boldsymbol{\theta} = [\boldsymbol{\Theta}\ \Delta\boldsymbol{\Theta}]^T$ of the system. The time evolution is then governed by a linear state transition equation

$$\boldsymbol{\theta}_k = \mathbf{F}_k \boldsymbol{\theta}_{k-1} + \mathbf{v}_k, \tag{2.11}$$

where $\mathbf{v}_k \sim \mathcal{N}(\mathbf{0}, \mathbf{Q}_k)$ is the state noise vector at time k. The measurement equation is defined as the nonlinear mapping of the state variables to the observation, i.e., the measured channel as

$$\mathbf{y}_k = \mathbf{h}(\boldsymbol{\theta}_k) + \mathbf{n}_k, \tag{2.12}$$

where $\mathbf{n}_k$ is the measurement noise vector. Both [SRK09] and [YSK+08] assume complex Gaussian entries for $\mathbf{n}_k$. However, in [SRK09], the measurement noise was colored due to the inclusion of the DMC (2.7), whereas [YSK+08] assumed white complex Gaussian noise (2.5).

The EKF relies on a Taylor series approximation for linearizing the nonlinear measurement equation (2.12) about the current parameter estimates. The computational complexity of the EKF solution is comparable to that of a single iteration of

the RIMAX algorithm, typically leading to about an order of magnitude improvement in terms of the overall computation time [SRE+06]. The EKF method has been applied for processing vast channel sounding data sets, and the results have been used for example in analyzing indoor scattering mechanisms in [PHS+09b].

The particle filter works by using a set of particles, drawn from the assumed probability densities of the parameter space, to approximate the joint distribution that best fits the observed measurements. The advantage of the method is that it is not restricted to Gaussian probability densities, and it allows the propagation paths to have some spread in the respective parameter domains. A method was presented in [YSK+08] to avoid a large number of closely separated particles due to typically highly concentrated paths. This method achieves a computational complexity lower than the SAGE algorithm.

Both EKF and particle filter-based sequential estimation approaches have been reported to outperform single-snapshot ML-based algorithms in terms of parameter estimation accuracy in simulations [YSK+08, SRE+06].

2.2.1.3 Clustering of Propagation Path Parameters

It is a widely accepted assumption that the propagation paths typically appear in so-called clusters. Clustering is also a convenient approach from the channel simulation point of view, as it provides a well-defined framework for drawing time-evolving channel realizations. Clustering has formed a basis for several standardized models, including COST 273 [Cor06].

In order to parameterize cluster-based channel models, it is necessary to perform clustering of the high-resolution propagation path parameter estimates and track them over time. Such an approach was proposed in [CTW+07], where a KPower-Means clustering algorithm using the Multipath Component Distance (MCD) distance metric [CCS+06] was suggested for clustering windows of data, and a Kalman filter was applied to predict and track the cluster positions over time. The authors in [CTW+07] also propose to use a so-called *closeness function* as a metric while associating the clusters over time. A 3D-illustration of the clustering results for a single time window is shown in Fig. 2.29. This clustering method was also employed in [ZTE+10] in order to parameterize a cluster-based channel model. A similar approach, but using particle filters for cluster tracking, was described in [SKI+10b].

An alternative clustering approach using the so-called *hierarchical whole clustering method* [JD88] was proposed in [KH08]. Comparing the results based on the two clustering approaches [CTW+07] and [KH08], it is evident that the definition of path clustering is somewhat ambiguous. Namely, the results in [KH08] indicate that the clusters have Root-Mean-Square (RMS) angular spreads in the order of one degree or even less. One can then argue whether such results are in fact uncertainty resulting from estimating and tracking a single propagation path instead of a cluster of paths, as the approach yields similar results as the sequential estimation algorithms (single-path tracking) [SRK09, YSK+08], where the association of the paths over time is implicitly obtained.

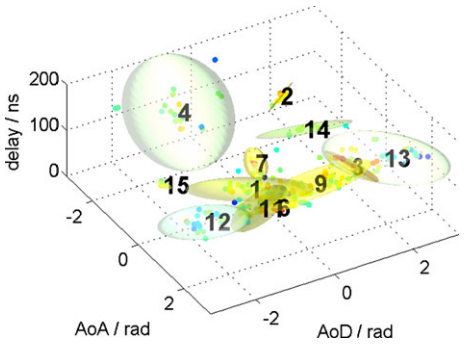

Fig. 2.29 An example of propagation path clustering in an indoor scenario [CTW+07] (©2007 IEEE, reproduced with permission)

As clustering is based on the estimated propagation paths which typically represent only a portion of the propagation channel, see, e.g., [RSK06, SCPF09], it can be hard to quantify in retrospect how much of the overall channel remains unaccounted for. Recently, a cluster-based model for the DMC was proposed in [SPH+10] to overcome this limitation. However, no method for automatic extraction of the parameters of such a model has been reported so far.

2.2.2 Scatterer Localization and Visualization

The development of radio channel models should always be based on thorough understanding of the physical propagation phenomena. To obtain this understanding, it is essential to identify underlying propagation mechanisms, such as reflections, diffraction, or scattering from physical objects of propagation environments. However, understanding all the relevant propagation mechanisms by manual comparison of the measurement results with the maps or photos of the environment is a cumbersome task. Therefore it is helpful to develop simple and efficient scatterer localization and visualization tools and methods. In this subsection four examples of such tools and methods are introduced [KH07, PHS+09a, CPD10, SKA+08, MB10]. Fundamental ideas of those tools and methods are to relate the data obtained from channel measurements to the physical scattering objects of the surrounding environment.

Poutanen et al. [PHS+09a] developed a so-called measurement-based ray tracer. The ray tracer combines a digital map of the environment with high-resolution directional parameter estimates obtained from the measurement data. The environment is described by representing surfaces of the objects by straight lines, and rays are plotted on top of the map from the locations of transmit and receive terminals. The directions of the rays are based on the measured Direction of Departure (DoD) and DoA, and the rays hit a surface of a certain object. In this way the scattering points and propagation paths of each multipath component can be identified. Figure 2.30 shows an example of identified scattering points from a double-directional propagation measurement in an indoor hall environment. The Transmitter (Tx) was

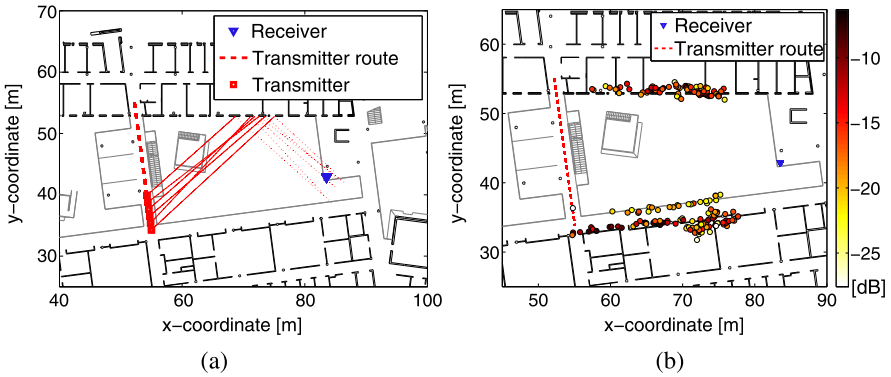

Fig. 2.30 Example of identifying propagation paths of rays in an indoor hall scenario using the measurement-based ray tracer: (**a**) Rays are launched from Tx to the direction of DoD, and a specular reflection is assumed to update the signal direction after the ray hits the wall. (**b**) Scattering points of single bounce paths on two walls. They are calculated by intersection of rays launched from Tx and Rx

moved along a route shown in a red dashed line, while the Receiver (Rx) was fixed. Figure 2.30(a) shows that rays are launched from consecutive Tx locations along a measurement route to the direction of the DoD, and hit a surface of a wall defined in an AutoCAD drawing of the environment. By calculating a specular reflection on the wall surface and by using the delay information of each multipath component, the rays arrive approximately at the Rx. Figure 2.30(b) shows scattering points calculated by the intersection point of rays launched from Tx and Rx for single-bounce paths from the two walls. The color of scattering points represents the relative power level of the rays. It is clearly seen on the map that the rays from scattering points between $y = 30$ and 40 m stem from both wall reflections and reflections from a fence along the corridor. In this way the measurement-based ray tracer enables us to analyze contributions of different propagation mechanisms and also to group multipaths originating from same scattering processes to form physically motivated clusters.

Kwakkernaat and Herben [KH07], Cornat et al. [CPD10], and Medbo [MB10] developed tools to plot measurement results on the photograph of the environment. The tool is a convenient way to physically analyze the channel behavior. In addition, since complex channel measurements are prone to errors, the tool can be used to verify the soundness of the measured data. The basic idea of the proposed approach is to generate a 3-D panoramic photograph by taking several photos that slightly overlap and stitch them together. A 3-D panoramic photograph covers 180 degrees in elevation and 360 degrees in azimuth, so it can be combined with the measured power angular spectrum and angles of propagation path parameter estimates that cover the same range. The combination of the 3-D panoramic photograph and the measured power angular spectrum is called a radiophoto in [CPD10]. Such a photograph was first reported in [KH07] for their macrocellular outdoor measurements in Eindhoven, the Netherlands, to plot parameter estimates from the 3-D Unitary ESPRIT as shown in Fig. 2.31(a). The photo was taken by a camera located directly

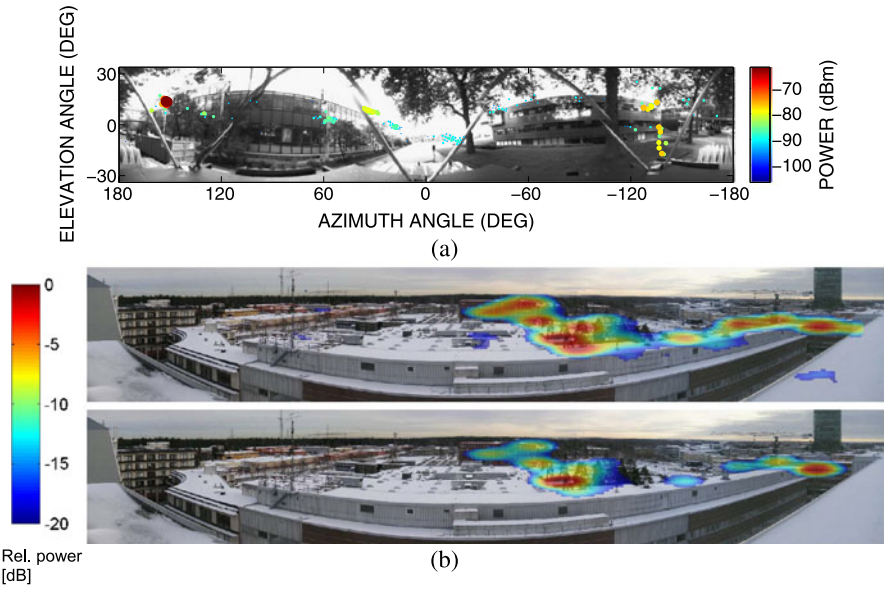

Fig. 2.31 (**a**) A photograph of a macrocellular environment seen from the MS, Eindhoven, the Netherlands. Propagation path estimates from the 3-D Unitary ESPRIT are overlaid on the photo. (**b**) Aggregate angular spectrum overlaid on a panoramic photo taken from the BS. The measurement was in a macrocellular scenario, Kista, Sweden

underneath a mobile antenna array that was mounted on a rooftop of a measurement vehicle. Similarly, a radiophoto obtained in an outdoor macrocellular scenario in the city center of Mulhous, France, is shown in [CPD10]. The photos clearly highlight the main propagation mechanisms, such as diffraction over the rooftops, reflections from surrounding buildings, and street canyons toward the direction of base station. The photo on the Base Station (BS) side was introduced in [MB10] for outdoor macrocellular scenario in Kista, Sweden, at 5.25 GHz as shown in Fig. 2.31(b). The angular power spectrum overlaid on the photo was derived by aggregating all the propagation paths estimated from 10 different Mobile Station (MS) locations. The power spectrum in the upper figure was obtained after removing the pathloss difference between BS-MS links, while that in the lower figure was derived with the link pathloss difference preserved. The photo revealed that propagation paths between the BS and the MSs were clustered in directions where building walls or roof edges have LOS conditions to both the BS and the MSs.

Santos et al. [SKA+08] established a method which identifies scatterers using successive interference cancellation (a detect-and-subtract method) for ultrawideband channel measurements. The novelty of the work is to map peaks of channel impulse responses detected in the delay domain to scatterers on the two-dimensional spatial domain. To this end, the channel measurement was carefully designed; a single Tx antenna was put on a fixed position, while a quite large array which stretched beyond the channel stationarity region was formed by moving a single antenna on

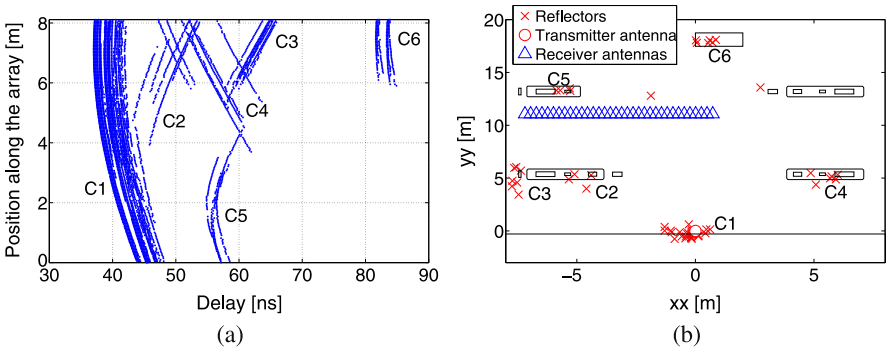

Fig. 2.32 Propagation path detection and scatterer identification in outdoor petrol station by ultrawideband channel sounding: (**a**) Detected scatterer peaks in the delay domain. (**b**) Map of the measurement scenario and the calculated spatial positions of scatterers. Petrol pumps and shop building are also shown [SKA+08] (©2008 IEEE, reproduced with permission)

the Rx side. The scatterer identification was made possible by assuming a single bounce of each scattered wave. An example of such measurements and scatterer identification is reported for outdoor measurements in a petrol station in Lund, Sweden. The scatterers were detected in the delay domain for successive Rx positions as shown in Fig. 2.32(a) and were related to the physical objects in the spatial domain as shown in Fig. 2.32(b). The position of Tx and Rx antennas as well as the most significant objects in the channel, such as the petrol pumps and the shop wall, are also shown. Almost all the scatterers identified in the measurements corresponded to physical objects, which was a strong indication that single-bounce reflections were dominating in this scenario. The method is, therefore, of great value for ultrawideband channel modeling and for automated generation of environment maps.

2.2.3 Impact of System Calibration

When conducting measurements of the mobile radio channel, it is important to keep in mind that the measurement data is always influenced by the measurement system. This means the data always contains both the actual channel transfer function $H(f,t)$ and the characteristics of the measurement system. Another very important aspect is the impact of the antenna arrays used during measurements. In general, the beampatterns of the arrays lead to a spatial filtering of the mobile radio channel. Thus, the measured channel transfer function can differ depending on the characteristics of the antennas. This influence can only be removed by high-resolution parameter estimation or to some extent by beamforming [WHR+10]. In order to perform these procedures, a precise knowledge of the antenna beampatterns is necessary.

2.2.3.1 Calibration of Receiver/Transmitter

In general, both the receiver and transmitter possess a frequency response that is not flat. This can be caused by, e.g., power amplifiers at the transmitter or low-noise amplifiers at the receiver. The impact on the measured transfer function of the radio channel is that it is multiplied with the transfer function of the receiver and transmitter, respectively:

$$\widehat{H}(f,t) = G_{sys,Rx}(f) \cdot H(f,t) \cdot G_{sys,Tx}(f), \tag{2.13}$$

where $G_{sys,Rx/Tx}$ are the time-independent transfer functions of the receiver and transmitter, respectively. Since the transfer functions of the measured device are assumed to be constant over time, it is possible to remove their impact by a single Back-2-Back system calibration. This procedure is performed by directly connecting the receiver and transmitter and conducting a measurement. The resulting transfer function $C(f)$ is then stored and later on used to get the estimate of the actual channel transfer function:

$$C(f) = G_{sys,Rx}(f) \cdot G_{sys,Tx}(f), \tag{2.14}$$

$$\widetilde{H}(f,t) = \frac{\widehat{H}(f,t)}{C(f)}. \tag{2.15}$$

Some measurement devices are equipped with an Automatic Gain Control (AGC) which controls the input power of the internal components of the system. This is useful in order to avoid any nonlinear effects of, e.g., amplifiers or analog-digital-converters. It is important to note that in this case it is necessary to perform the Back-2-Back calibration for each of the different AGC settings. The necessity to perform a Back-2-Back system calibration stems from the purpose of a channel sounder to measure the transfer function of the radio channel without the influence of the measurement system as accurately as possible. In an actual communication system, on the other hand, there is no need to separate the radio channel from the receiver or transmitter system; instead they can be treated jointly. For the communications systems, it is only important that there is a frequency-selective transfer function, but it is not important whether the frequency selectivity arises from the multipath propagation in the environment or is induced by the RF-components of the receiver or transmitter.

Nevertheless, it is still necessary to measure the (joint) channel transfer function. This information (channel state information) is later used to equalize the influence of the total channel (e.g., in an OFDM-System) or is used to exploit certain properties of the channel (like water pouring in a MIMO system). Since the RF-components of the transmitter and receiver are in general not identical, it is necessary to measure both the downlink (transmitter to receiver) and the uplink (receiver to transmitter). The information of, e.g., the uplink is then transferred back to the transmitter to get the full CSI. If the uplink and downlink are reciprocal, the knowledge about either of them can be obtained by a procedure called relative calibration [KJGK10].

As stated above, the transfer function of the measurement device is presumed to be time invariant. While this is true for the magnitude, it might not be correct for the phase. Each system is affected by phase noise and phase drift of the receiver and transmitter, respectively. If this is not accounted for by different means, for example, by using a reference channel or highly stable reference signals, it might *pretend* a variation of the radio channel, thus leading to overestimation of metrics like channel capacity [CO09]. If no reference signal can be used, the impact on channel analysis depends on the magnitude of the phase noise. Since channel sounding measurements are conducted with highly specialized equipment, it can be assumed that the strength of the phase noise is low. In [GKT10b] Ghoraishi et al. used an OFDM-based channel sounder with the phase noise magnitude lower than -60 dBc/Hz to investigate the influence of phase variations. They used simulations and measurements to show that the impact of the phase noise on the channel impulse response can be neglected when the magnitude is below -50 dBc/Hz.

2.2.3.2 Calibration of Antenna Arrays

In the previous section the influence of the RF-components (of both the receiver and transmitter) on the frequency response of the system was discussed. Its impact can easily be equalized by applying some sort of system calibration. Another important aspect of channel measurements is the influence of the antenna arrays, particularly the influence of the spatial directivity of the individual array elements. In order to compensate for the effects of the antennas, it is common to perform high-resolution parameter estimation (see Sect. 2.2.1). This procedure is able to "deembed" the antennas from the channel measurements. One prerequisite of any estimator is the availability of the beam patterns of the antenna arrays. It is apparent that the quality of any subsequent parameter estimate is limited by the accuracy of the beam pattern. The beam pattern is usually obtained by measuring the response of an array inside an anechoic chamber. The accuracy of the beam patterns is, however, limited by the actual calibration procedure. Although the measurement is performed in an anechoic chamber, multipath propagation can still occur, although it is only attenuated to a certain level. Depending on the nature of these multipath (e.g., reflections close to the antenna under test), the measurements can be irreversibly distorted. In order to quantify the impact of the distortion, a measure about the quality of the data is required. In [KT10] it is suggested to use the measured beam patterns during a parameter estimation of a reference measurement—such as the calibration measurement itself—and to evaluate the accuracy of the estimation.

Besides these inherent limitations, the beam patterns are, however, often deliberately restricted in order to reduce the computational complexity of the estimation process or because of assumptions that are made about the radio channel or about the properties of the antenna arrays. Some of these assumptions are:

1. nominal single-polarized antennas with high Cross-Polar Discrimination (XPD) in the main-beam direction will keep the same XPD for different angle of arrival

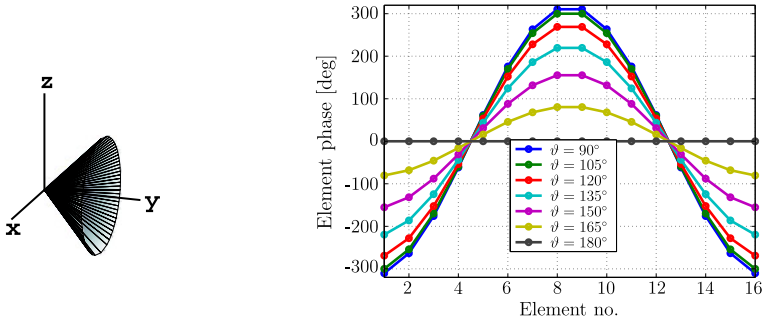

(a) DoAs that result in the same phase constellation at an ideal ULA (elements placed along y-axis, $\Delta\alpha = 45°$)

(b) Phase over 16 element UCA, ∅ 10.5 cm at 5.2 GHz for incidence at different co-elevations ϑ.

Fig. 2.33 Phase over 16-element UCA (©2007 EurAAP, reproduced with permission)

2. nominal uniform arrays exhibit equal beam patterns for all elements, thus ignoring mutual coupling
3. if only azimuthal properties are to be examined, it is sufficient to use only azimuthal "cuts" of the full-3D beam pattern
4. if an array is used that cannot resolve the Elevation of Arrival (EoA), the estimates of the AoA are still correct

It must be said that the last assumption is different from the others in the sense that it cannot be resolved by using the full polarimetric 3D beam pattern; in fact, it is a consequence of the choice of the array used. If these assumptions are violated—which is nearly always the case with practical arrays—and still the restricted beam patterns are used, it can lead to biased estimates or even cause artifacts that do not reflect the radio channel [LKT07]. Especially the emergence of artifacts is harmful since it may pretend clusters in the propagation environment, which are not physically correct.

The ULA is a type of antenna array that reveals the consequences of the fourth assumption. Since it is ambiguous with respect to the elevation angle, it is often only used to examine the AoA, thus, using only an azimuthal cut of the beam pattern. The ambiguity of the ULA lies in its inability to resolve any paths in the elevation domain. Nevertheless, that does not mean that the beam pattern of the ULA will not change with elevation. This is particularly true for the phase variation over the array elements. This phase variation is the most important information for an estimator to determine the direction of the impinging wave. If the phase variation over the elements is unique for all pairs of angles in azimuth and elevation, the array is unambiguous. If there are multiple pairs of angles that lead to the same phase pattern, it is impossible to reliably decide which angle is the correct one. In Fig. 2.33 one can see the "ambiguity-cone" of the ULA. It shows that any impinging wave whose direction of arrival is on this cone will lead to the same phase pattern on the array elements. If an azimuthal cut of the beam pattern is used and the cut is not performed for the correct elevation angle, this will lead to biased estimates for the azimuth angle. Note that this problem can only be solved for the ULA by suppressing waves

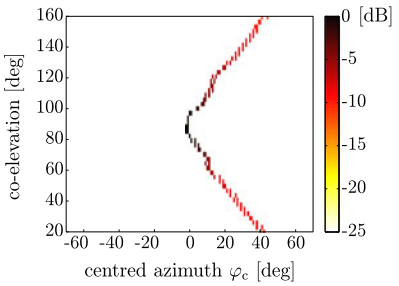

(a) Horizontal excitation, azimuth of the true path $\varphi = -70°$.

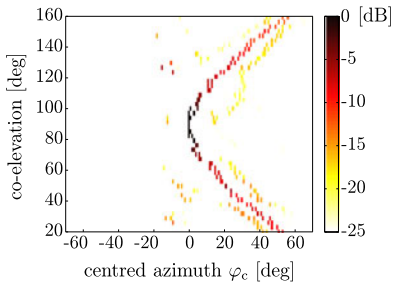

(b) Vertical excitation, azimuth of the true path $\varphi = -70°$.

Fig. 2.34 Power distributions of the estimated paths as function of the centered azimuth (estimation bias) around the true path and co-elevation using the full polarimetric 1D data model of a 8-element ULA for $\varphi = -70°$ of the true path from top to bottom and for horizontal (*left*) and vertical excitation (*right*) [LKT07] (©2007 EurAAP, reproduced with permission)

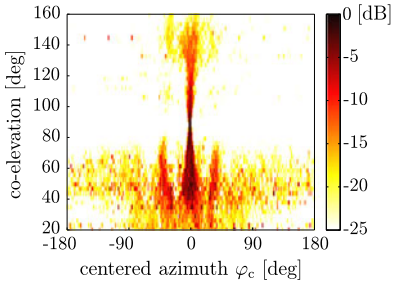

Fig. 2.35 Estimation artifacts (bias) around the true path using the azimuth-only data model of a UCA [LKT07] (©2007 EurAAP, reproduced with permission)

with other elevation angles already during the measurements. A better approach is to use a Uniform Circular Array (UCA) where the phase variation is unique, at least for one hemisphere of the spherical coordinate system, or to use a stacked UCA or other three-dimensional array configurations. Figure 2.34 shows some examples of estimation results using a ULA where estimations where performed with azimuth-only beam patterns that where derived for an elevation angle (90° coelevation in this case) that do not match the elevation angles of the actual propagation paths. It can be seen that the AoA is only estimated correctly for a coelevation of 90°, which is the angle where the EoA of the impinging wave matches the EoA of the azimuth-only beam pattern. It can be seen that although the bias of the estimates is sometimes high, the spread, i.e., the estimation artifacts around the true path, is relatively small. This is caused by the ambiguity of the ULA. In other words, within the 1D-beam pattern, there exists a phase pattern that, although belonging to a different combination of AoA and EoA (compared to the true parameters) allows the estimator to find a proper match with the received signal. If an array type is used that does not have this property and still a 1D-beam pattern is used, the situation is completely different. Figure 2.35 shows the estimation artifacts that arise when a UCA is used with only a 1D-beam pattern. In this case it is not possible for the estimator to find a suitable phase pattern within the 1D-beam pattern if the EoA of the impinging

wave is different from the EoA the 1D-beam pattern was created for. This causes the estimator to introduce additional artificial paths to match the received signal.

Concluding, the impact of both the array calibration accuracy and the simplification of the data model depend heavily on the types of analyses or simulations that are to be performed using the parameter estimates. In [EWLT10] the authors investigated the reliability of estimation results by synthesizing channels and comparing them to actual measurement data. It was found that a good agreement w.r.t. to power and MIMO channel capacity can be achieved. However, using this approach, it is not always possible to determine the physical relevance of the estimated propagation parameters, since the authors used the same antenna array (array calibration data) for the synthesis that was used for the estimation. The estimation procedure aims to describe the measured data as accurately as possible, and if the accuracy of the array calibration data is limited, the estimator will compensate for this by introducing artifacts. Thus, a synthesis using the same (limited) calibration data will again lead to an accurate-as-possible description of the measurement data. Therefore, the estimation results in [EWLT10] are also validated using visual inspection showing some possibilities of estimation artifacts. In [KSKT10] measurement data is used to derive an antenna-independent description of the radio channel and to synthesize data for a different antenna. The accuracy of the synthesis is again verified using the MIMO channel capacity. Since a different array is used for the synthesis, the impact of estimation artifacts can be observed in the results. It is furthermore shown that the impact of the estimation errors increases with rising SNR of the simulations. Therefore, it can be concluded that the calibration of the measurement devices and the validity of the data model ultimately limit the usefulness of any subsequent processing of the data.

2.3 Lessons Learned

The previous paragraphs presented a technical overview of the wide range of activities done in the field of radio channel measurements. This last part shall give a short insight into the practical problems when planning new field measurements. No matter for which kind of technology the radio measurements shall be done, there are a number of basic points to be always considered before starting out.

- *Focus of the measurements*—The most important thing that one should ask oneself before a measurement campaign is: What do I expect to learn from the measurements? Only after having a clear and concise answer to this question, meaningful measurements can be designed. This may sound straightforward, however, it happened in the past that measurements have been performed without a defined focus, which obviously lead to quite limited results.
- *Equipment*—Given the focus, one needs to decide which equipment can fulfill the needs. For already existing specialized measurement equipment, it might turn out that it does not fit the purpose. In this case, either the focus or the equipment need to be updated.

Furthermore, recent experience showed that combining specialized channel sounding equipment of different makes is extremely challenging and time consuming. It is of great importance to test the equipment thoroughly before going to the field trials. Every glitch that is not captured before the measurements multiplies time and cost of postprocessing.

It is also necessary to plan for additional tools and items, like connectors, converters, extension cords, but also for cars, gas, power generation, or simply for having a great supply of duct tape.

- *Schedule*—Allow and plan for enough time. In the preparations, the exact measurement locations, equipment settings, and measurement parameters should be defined. This may also involve doing some sample measurements before the campaign starts to adjust the parameters. No doubt, the planning of a campaign takes much longer than the measurement campaign itself.

  For the period of the campaign also include some extra time in your planning for solving unforeseen problems. Measurement equipment is generally error-prone since it is usually experimental equipment. Having a specialized channel sounder at hand usually helps a lot but does not completely prevent faults from happening.

  Finally, the large amounts of data collected need to be evaluated. One should already have a time schedule for the evaluations agreed as well.
- *Documentation*—Meaningful documentation is the most essential part of every measurement campaign. What does an abundance of data help if one does not know where (and with which parameter settings) it was collected? Using so-called "field note sheets" is encouraged, where the measurement location, settings, possible photographs, and other important information can be written during the measurement.
- *People*—Having enough helpers makes life much easier. Distributing tasks (coordination, documentation, measuring, assisting the measurement team) allows everybody to focus on their part and leaves the coordinator to oversee and guide the action.

As a final comment, radio channel measurements are always a challenge, but when keeping to a well-prepared plan, the results merit the efforts.

References

[AAM09] A. Adalan, H. Arthaber, and C. Mecklenbraeuker. On the potential of IEEE 802.15.4a for use in car safety and healthcare applications. Technical Report TD-09-865, Valencia, Spain, May 2009.

[AFG+09] A. Adalan, M. Fischer, T. Gigl, K. Witrisal, A. L. Scholtz, and C. F. Mecklenbraeuker. Ultra-wideband radio pulse shaping filter design for IEEE 802.15.4a transmitter. In *Proc. WCNC 2009—IEEE Wireless Commun. and Networking Conf.*, Budapest, Hungary, April 2009.

[AGFW09] A. Adalan, T. Gigl, M. Fischer, and K. Witrisal. A modular impulse radio ultra-wideband research & development platform for IEEE 802.15.4a. In *European Conference on Wireless Technologies, ECWT*, pages 116–119, Rome, Italy, September 2009.

[ASQ09] J. Ahmadi-Shokouh and R. C. Qiu. Ultra-wideband (UWB) communications channel measurements—a tutorial review. *Int. J. Ultra Wideband Communications and Systems*, 1(1):11–31, 2009.

[BDHZ10] R. J. C. Bultitude, G. S. Dahman, R. H. M. Hafez, and H. Zhu. Double directional radio propagation measurements and radio channel modelling pertinent to mobile MIMO communications in microcells. Technical Report TD-10-11019, Aalborg, Denmark, June 2010.

[BLM04] J. R. Barry, E. A. Lee, and D. G. Messerschmitt. *Digital Communication*, 3rd edition. Kluwer, Boston, USA, 2004.

[BS87] P. Beckmann and A. Spizzichino. *The Scattering of Electromagnetic Waves from Rough Surfaces*. Artech House, Norwood, 1987.

[CAS08] L. Clavier, N. Azzaoui, and W. Sawaya. UWB and 60 GHz channel model as an α-stable random process. Technical Report TD(08)634, Lille, France, October 2008.

[CBVV+08a] N. Czink, B. Bandemer, G. Vazquez-Vilar, L. Jalloul, and A. Paulraj. Can multi-user MIMO measurements be done using a single channel sounder? Technical Report TD-08-621, Lille, France, October 2008.

[CBVV+08b] N. Czink, B. Bandemer, G. Vazquez-Vilar, L. Jalloul, and A. Paulraj. Stanford July 2008 radio channel measurement campaign. Technical Report TD-08-620, Lille, France, October 2008.

[CCC10a] Q. Chu, J.-M. Conrat, and J.-C. Cousin. On the impact of receive antenna height in a LTE-advanced relaying scenario. Technical Report TD-10-11005, Aalborg, Denmark, June 2010.

[CCC10b] Q. Chu, J.-M. Conrat, and J.-C. Cousin. Path loss characterization for LTE-advanced relaying propagation channel. Technical Report TD-10-12019, Bologna, Italy, November 2010.

[CCL+10] P. Chambers, P. Castiglione, L. Liu, F. Mani, F. Quitin, O. Renaudin, F. Sanchez-Gonzales, N. Czink, and C. Oestges. PUCCO radio measurement campaign. Technical Report TD-10-11015, Aalborg, Denmark, June 2010.

[CCS+06] N. Czink, P. Cera, J. Salo, E. Bonek, J.-P. Nuutinen, and J. Ylitalo. A framework for automatic clustering of parametric MIMO channel data including path powers. In *Proc. VTC 2006 Fall—IEEE 64th Vehicular Technology Conf.*, Montreal, Canada, September 2006.

[cha10] MEDAV RUSK channel sounder, 2010. http://www.channelsounder.de.

[CO09] N. Czink and C. Oestges. Impacts of channel sounder phase noise (forum discussion). Technical Report TD-09-738, Braunschweig, Germany, February 2009.

[Cor06] L. M. Correia, editor. *Mobile Broadband Multimedia Networks*. Academic Press, San Diego, 2006.

[CPB07] R. Cepeda, S. C. J. Parker, and M. Beach. The measurement of frequency dependent path loss in residential LOS environments using time domain UWB channel sounding. In *IEEE Intern. Conf. on Ultra-Wideband, ICUWB*, Singapore, September 2007. [Also available as TD(07)306].

[CPD10] J.-M. Conrat, P. Pajusco, and A. Dunand. On the use of panoramic photography for understanding propagation channel physical phenomena. Technical Report TD(10)12024, Bologna, Italy, November 2010.

[CTB08] R. Cepeda, W. Thompson, and M. Beach. On the mathematical modelling and spatial distribution of UWB frequency dependency. In *2008 IET Seminar on Wideband and Ultrawideband Systems and Technologies: Evaluating Current Research and Development*, pages 1–5, November 2008. [Also available as TD(08)456].

[CTT+09] C. Cordeiro, S. Trainin, J. Trachewsky, S. Shankar, Y. Liu, G. Basson, and J. Yee. Implications of usage models on TGad network architecture. In *IEEE Doc. 802.11-09/0391r0*, Vancouver, BC, Canada, March 2009.

[CTW+07] N. Czink, R. Tian, S. Wyne, F. Tufvesson, J.-P. Nuutinen, J. Ylitalo, E. Bonek, and A. F. Molisch. Tracking time-variant cluster parameters in MIMO channel measurements. In *The 2nd International Conference on Communications and Networking*

in China (CHINACOM 2007), pages 1147–1151, August 2007. [Also available as TD(07)336].

[CZZ04] S. Collonge, G. Zaharia, and G. E. Zein. Influence of the human activity on wide-band characteristics of the 60 GHz indoor radio channel. *IEEE Transactions on Wireless Communications*, 3(6):2396–2406, 2004.

[DC08] A. Dunand and J.-M. Conrat. Polarization behaviour in urban macrocell environments at 2.2 GHz. Technical Report TD-08-406, Wroclaw, Poland, February 2008.

[ECC03] ECC. The european table of frequency allocations and utilizations covering the frequency range 9 kHz to 275 GHz. In *ERC Report 25*, pages 1–268, Dublin, Ireland, January 2003.

[ECM08] ECMA. High rate 60 GHz PHY, MAC and HDMI PAL. In *ECMA-387*, 1st edition, pages 1–344, Geneva, Switzerland, December 2008.

[Ele10] Elektrobit EB Propsim Homepage. 2010. http://www.propsim.com.

[ETM07] G. Eriksson, F. Tufvesson, and A. F. Molisch. Characteristics of MIMO peer-to-peer propagation channels at 300 MHz. Technical Report TD-07-376, Duisburg, Germany, September 2007.

[EWLT10] G. Eriksson, K. Wiklundh, S. Linder, and F. Tufvesson. Directional channel estimates from urban peer-to-peer MIMO measurements at 285 MHz. Technical Report TD-10-12099, Bologna, Italy, November 2010.

[FCC01] FCC. Part 15-radio frequency devices section 15.255: operation within the band 57.0–64.0 GHz. In *Code of Federal Regulations*, pages 1–762, USA, January 2001.

[FCC02] FCC. Revision of part 15 of the commission's rules regarding ultra-wideband transmission systems. First Report and Order, ET Doc. 98-153, FCC 02-48, Adopted: February 14, 2002, Released: April 22, 2002.

[FS10] S. Feeney and S. Salous. Implementation of a channel sounder for the 60 GHz band. Technical Report TD-10-10043, Athens, Greece, February 2010.

[FTH+99] B. H. Fleury, M. Tschudin, R. Heddergott, D. Dahlhaus, and K. I. Pedersen. Channel parameter estimation in mobile radio environments using the SAGE algorithm. *IEEE J. Select. Areas Commun.*, 17(3):434–450, 1999.

[Gar10] A. Garcia. The 60 GHz in-cabin channel. In *IEEE Doc. 802.11-10/0027r0*, pages 1–32, Los Angeles, CA, USA, January 2010.

[GBA+09] T. Gigl, T. Buchgraber, A. Adalan, J. Preishuber-Pfluegl, M. Fischer, and K. Witrisal. UWB channel characterization using IEEE 802.15.4a demonstrator system. In *IEEE Intern. Conf. on Ultra-Wideband, ICUWB*, pages 230–234, Vancouver, Canada, September 2009.

[GBG+09] T. Gigl, T. Buchgraber, B. Geiger, A. Adalan, J. Preishuber-Pfluegl, and K. Witrisal. Pathloss and delay spread analysis of multipath intensive environments using IEEE 802.15.4a UWB signals. Technical Report, Vienna, Austria, September 2009. [TD(09)965].

[GKBT09] A. P. Garcia, W. Kotterman, D. Brückner, and R. S. Thomä. 60 GHz in-cabin channel characterisation and human body effects. Technical Report TD-09-756, Braunschweig, Germany, February 2009.

[GKKV10] S. Geng, M. Kyrö, V.-M. Kolmonen, and P. Vainikainen. Feasibility Study of E-band Radio for Gigabit Point-to-Point Wireless Communications. Technical Report TD(10)10076, Athens, Greece, February 2010.

[GKT+09] A. P. Garcia, W. Kotterman, R. S. Thomä, U. Trautwein, D. Brückner, W. Wirnitzer, and J. Kunisch. 60 GHz in-cabin real-time channel sounding. In *Proc. Fourth Int. Conf. on Commun. and Networking in China (ChinaCOM2009)*, pages 1–5, Xi'an, China, 2009. [Also available as TD(09)877].

[GKT+10a] A. P. Garcia, W. Kotterman, U. Trautwein, D. Brückner, J. Kunisch, and R. S. Thomä. 60 GHz time-variant shadowing characterization within an Airbus 340. In *Prod. 4th European Conf. on Antennas and Propagation (EuCAP 2010)*, pages 1–5, Barcelona, Spain, 2010. [Also available as TD(09)970].

[GKT10b] M. Goraishi, M. Kim, and J. Takada. Influence of phase noise on the frequency division multiplexing channel sounding. Technical Report TD-10-12044, Bologna, Italy, November 2010.

[GKZ+10] A. P. Garcia, W. Kotterman, R. Zetik, M. Kmec, R. Müller, F. Wollenschläger, U. Trautwein, and R. S. Thomä. 60 GHz-ultrawideband real-time multi-antenna channel sounding for multi giga-bit/s access. In *IEEE 72nd Vehicular Technology Conference (VTC-Fall 2010)*, pages 1–6, Ottawa, Canada, September 2010. [Also available as TD(10)11090].

[GM+10] A. P. Garcia, R. Müller, F. Wollenschläger, L. Xia, A. Schulz, M. Elkhouly, Y. Sun, U. Trautwein, and R. S. Thomä. Dual-polarized architecture for ultrawideband channel sounding at 60 GHz with digital/analog phase control based on 0.25 mm SiGe BiCMOS and LTCC technology. Technical Report TD-10-12015, Bologna, Italy, November 2010.

[GR07a] R. Goossens and H. Rogier. 2-D direction-of-arrival estimation in the presence of mutual coupling by exploiting the symmetry in uniform circular array. Technical Report TD-07-214, Lisbon, Portugal, February 2007.

[GR07b] R. Goossens and H. Rogier. Improved root-music based 2-d DOA estimation algorithm by considering a cylindrical antenna array configuration. Technical Report TD-07-370, Duisburg, Germany, June 2007.

[GTPPW10] T. Gigl, F. Troesch, J. Preishuber-Pfluegl, and K. Witrisal. Maximal operating distance estimation using IEEE 802.15.4a ultra wideband. In *Workshop on Positioning, Navigation, and Communication, WPNC*, Dresden, Germany, March 2010.

[GTS+10] D. P. Gaillot, E. Tanghe, P. Stefanut, W. Joseph, M. Lienard, P. Degaque, and L. Martens. Accuracy of specular path estimates with ESPRIT and RiMAX in the presence of diffuse multipath. Technical Report TD-10-12022, Bologna, Italy, November 2010.

[GTWH10] C. Gustafson, F. Tufvesson, S. Wyne, and K. Haneda. Directional analysis of measured 60 GHz indoor radio channels in a conference room. Technical Report TD-10-12077, Bologna, Italy, November 2010.

[GWF+10] A. P. Garcia, F. Wollenschläger, S. M. Feeney, S. Salous, and R. S. Thomä. 60 GHz channel sounding based on frequency-modulated-continuous-wave techniques. Technical Report TD-10-10009, Athens, Greece, February 2010.

[HBH03] M. P. M. Hall, L. W. Barclay, and M. T. Hewitt. *Propagation of Radiowaves*, 2nd edition. Institution of Electrical Engineers, Inspec/IEE, 2003.

[HKY+05] L. Hentilä, P. Kyösti, J. Ylitalo, X. Zhao, J. Meinilä, and J.-P. Nuutinen. Experimental characterization of multi-dimensional parameters at 2.45 and 5.25 GHz indoor channels. In *WPMC2005*, Aalborg, Denmark, 2005. See also http://www.propsim.com/.

[HZMN95] M. Haardt, M. D. Zoltowski, C. P. Mathews, and J. Nossek. 2D unitary ESPRIT for efficient 2D parameter estimation. In *Proc. ICASSP 1995—IEEE Int. Conf. Acoust. Speech and Signal Processing*, vol. 3, pages 2096–2099. Detroit, MI, May 1995.

[IEE04] IEEE standard for local and metropolitan area networks part 16: Air interface for fixed broadband wireless access systems, 2004.

[IEE07] IEEE P802.15.4a-2007 (Amendment 1). 802.15.4: Wireless medium access control (MAC) and physical layer (PHY) specifications for low-rate wireless PANs, 2007.

[IEE09] IEEE. Part 15.3: wireless medium access control MAC and physical layer PHY specifications for high rate wireless personal area networks WPANs: Amendment 2: millimeter-wave based alternative physical layer extension. In *IEEE P802.15.3c/D02*, pages 1–194, New York, USA, July 2009.

[IEE10] IEEE. Part 11: wireless LAN medium access control (MAC) and physical layer (PHY) specifications, amendment 6: Enhancements for very high throughput in the 60 GHz band. In *IEEE P802.11ad/D0.1, Unapproved Draft*, pages 1–357, New York, USA, June 2010.

[IR03] ITU-R. Specification attenuation model for rain for use in prediction methods. In *Recommendation ITU-R P.838-2*, 2003.

[JD88] A. K. Jain and R. C. Dubes, editors. *Algorithms for Clustering Data*. Prentice Hall, New York, 1988.

[JJT+09] V. Jungnickel, S. Jaeckel, L. Thiele, L. Jiang, U. Kruger, A. Brylka, and C. von Helmolt. Capacity measurements in a cooperative MIMO network. *IEEE Trans. Veh. Technol.*, 58(5):2392–2405, 2009. [Also available as TD(09)730].

[JK09] M. Jacob and T. Kürner. Radio channel characteristics for broadband WLAN applications between 67 and 110 GHz. In *Proc. The Third European Conference on Ant. and Prop. (EuCAP)*, pages 1–5, Berlin, Germany, March 2009. [Also available as TD(09)745].

[JMK10] M. Jacob, C. Mbianke, and T. Kürner. A dynamic 60 GHz radio channel model for system level simulations with MAC protocols for IEEE 802.11ad. In *Proc. IEEE International Symposium on Consumer Electronics ISCE*, Berlin, Germany, June 2010. [Also available as TD(10)1109].

[JPJ+09] M. Jacob, S. Priebe, C. Jastrow, T. Kleine-Ostmann, T. Schrader, and T. Kürner. An overview of ongoing activities in the field of channel modeling, spectrum allocation and standardization for mm-Wave and THz indoor communications. In *Proc. Globecom 2009—IEEE Global Telecommunications Conf.*, pages 1–5, Honolulu, HI, USA, December 2009. [Also available as TD(10)10055].

[KAK+07] J. Koivunen, P. Almers, V.-M. Kolmonen, J. Salmi, A. Richter, F. Tufvesson, P. Suvikunnas, A. Molisch, and P. Vainikainen. Dynamic multi-link indoor MIMO measurements at 5.3 GHz. In *Proc. of EuCAP 2007*, 2007.

[KAS+] V.-M. Kolmonen, P. Almers, J. Salmi, J. Koivunen, K. Haneda, A. Richter, F. Tufvesson, A. F. Molisch, and P. Vainikainen. A dynamic dual-link wideband MIMO channel sounder for 5.3-GHz. *IEEE Trans. Instrum. Meas.*, **59**(4):873–883.

[KdJBH08] M. Kwakkernaat, Y. de Jong, R. Bultitude, and M. Herben. High-resolution angle-of-arrival measurements on physically-nonstationary mobile radio channels. *IEEE Trans. Antennas Propagat.*, 56(8):2720–2729, 2008.

[KGL+10] F. Kaltenberger, R. Ghaffar, I. Latif, R. Knopp, D. Nusbaum, and H. Callewaert. Comparison of LTE transmission modes in rural areas at 800 MHz. Technical Report TD-10-12080, Bologna, Italy, November 2010.

[KH07] M. Kwakkernaat and M. Herben. Analysis of clustered multipath estimates in physically nonstationary radio channels. In *Proc. PIMRC 2007—IEEE 18th Int. Symp. on Pers., Indoor and Mobile Radio Commun.*, pages 1–5, Athens, Greece, September 2007. [Also available as TD(07)324].

[KH08] M. R. J. A. E. Kwakkernaat and M. H. A. J. Herben. Analysis of scattering in mobile radio channels based on clustered multipath estimates. *Int. J. Wireless Inf. Networks*, 15(3–4):107–116, 2008. [Also available as TD(07)324].

[KHH+10] V.-M. Kolmonen, K. Haneda, T. Hult, J. Poutanen, F. Tufvesson, and P. Vainikainen. Measurement-based evaluation of interlink correlation for indoor multi-user MIMO channels. Technical Report TD-10-10070, Athens, Greece, February 2010.

[KHS+10] M. Kyrö, K. Haneda, J. Simola, P. Vainikainen, K. Takizawa, and H. Hagiwara. 60 GHz radio channel measurements and modelling in hospital environments. Technical Report TD-10-11049, Aalborg, Denmark, June 2010.

[Kiv07] J. Kivinen. 60 GHz wideband radio channel sounder. *IEEE Trans. Instrum. Meas.*, 56(5):1266–1277, 2007.

[KJ09] T. Kürner and M. Jacob. Application of ray-tracing to derive channel models for future multi-gigabit-systems. In *Proc. International Conference on Electromagnetics in Advanced Applications (ICEAA)*, pages 1–4, Torino, Italy, September 2009.

[KJGK10] F. Kaltenberger, H. Jiang, M. Guillaud, and R. Knopp. Relative channel reciprocity calibration in MIMO/TDD systems. In *Proc. ICT Future Network and Mobile Summit*, Florence, Italy, June 2010. [Also available as TD(09)950].

[KKC+08] F. Kaltenberger, M. Kountouris, L. S. Cardoso, R. Knopp, and D. Gesbert. Capacity of linear multi-user MIMO precoding schemes with measured channel data. In *Proc. IEEE Intl. Workshop on Signal Processing Advances in Wireless Communications (SPAWC)*, Recife, Brazil, July 2008. [Also available as TD(08)407].

[KLT09] M. Käske, M. Landmann, and R. Thomä. Modelling and synthesis of dense multipath propagation components in the angular domain. In *3rd European Conference on Antennas and Propagation (EuCAP 2009)*, pages 2641–2645, Berlin, Germany, March 2009. [Also available as TD(09)762].

[KMGT09] Y. Konishi, L. Materum, M. Ghoraishi, and J.-i. Takada. Multipath cluster polarization characteristics of a small urban MIMO macrocell. Technical Report TD-09-737, Braunschweig, Germany, February 2009.

[KSH+10] M. Kyrö, J. Simola, K. Haneda, S. Ranvier, P. Vainikainen, and K. Takizawa. 60 GHz radio channel measurements and modeling in a shielded room. In *IEEE 71st Vehicular Technology Conference (VTC-Spring 2010)*, pages 1–5, Taipei, Taiwan, May 2010. [Also available as TD(09)980].

[KSKT10] M. Käske, C. Schneider, W. Kotterman, and R. Thomä. Solving the problem of choosing the right MIMO sounding antenna: embedding/de-embedding. Technical Report TD-10-12081, Bologna, Italy, November 2010.

[KSP+05] M. Kmec, J. Sachs, P. Peyerl, P. Rauschenbach, R. Thomae, and R. Zetik. A novel ultra-wideband real-time MIMO channel sounder architecture. In *28th General Assembly of the International Union of Radio Sciences (URSI)*, New Delhi, India, October 2005.

[KST08] W. Kotterman, G. Sommerkorn, and R. Thomä. Ilmenau measurement data for SIG A. Technical Report TD-08-446, Wroclaw, Poland, February 2008.

[KT10] M. Käske and R. Thomä. Validation of estimated dense multipath components with respect to antenna array calibration accuracy. In *Proc. 4th European Conference on Antennas and Propagation (EuCAP 2010)*, Barcelona, Spain, April 2010. [Also available as TD(10)10075].

[LCK06] Z. Lei, F. Chin, and Y.-S. Kwok. UWB ranging with energy detectors using ternary preamble sequences. In *Proc. WCNC 2006—IEEE Wireless Commun. and Networking Conf.*, pages 872–877, 2006. doi:10.1109/WCNC.2006.1683585.

[LKT07] M. Landmann, W. Kottermann, and R. Thomä. On the influence of incomplete data models on estimated angular distributions in channel characterisation. In *Proc. 2nd European Conference on Antennas and Propagation (EuCAP 2007)*, Edinburgh, UK, November 2007. [Also available as TD(07)321].

[LMF10] B. K. Lau, J. Medbo, and J. Furuskog. Downlink cooperative MIMO in urban macrocell environments. In *Proc. IEEE Int. Symp. Antennas Propagat. (APS'2010)*, 2010.

[LSD+09] M. Lienard, E. Simon, P. Degauque, J.-M. Molina-Garcia-Pardo, and L. Juan-Llacer. Polarization diversity and MIMO capacity in tunnels. Technical Report TD-09-802, Valencia, Spain, May 2009.

[MB10] J. Medbo and J.-E. Berg. Directional propagation characteristics at the base station. Techical Report TD(10)12096, Bologna, Italy, November 2010.

[MFP+08] J. Maurer, T. Fügen, M. Porebska, T. Zwick, and W. Wiesbeck. A ray-optical channel model for mobile to mobile communications. Technical Report TD(08)430, Wroclaw, Poland, February 2008.

[MGPRJL08] J.-M. Molina-Garcia-Pardo, J.-V. Rodrıguez, and L. Juan-Llacer. Polarized indoor MIMO channel measurements at 2.45 GHz. Technical Report TD-08-605, Lille, France, October 2008.

[Mol09] A. F. Molisch. Ultra-wide-band propagation channels. *Proc. IEEE*, 97(2):353–371, 2009. doi:10.1109/JPROC.2008.2008836.

[MRAB05] J. Medbo, M. Riback, H. Asplund, and J. Berg. MIMO channel characteristics in a small macrocell measured at 5.25 GHz and 200 MHz bandwidth. In *Proc. VTC 2005 Fall—IEEE 62nd Vehicular Technology Conf.*, pages 372–376, Dallas, TX, September 2005.

[MSKF10] J. Medbo, I. Siomina, A. Kangas, and J. Furuskog. Propagation channel impact on LTE positioning accuracy—a study based on real measurements of observed time difference of arrival. Technical Report TD-10-11079, Aalborg, Denmark, June 2010.

[NKJ+10] M. Narandžić, M. Käske, S. Jäckel, G. Sommerkorn, C. Schneider, and R. S. Thomä. Variation of estimated large-scale MIMO channel properties between repeated measurements. Technical Report TD-10-11088, Aalborg, Denmark, June 2010.

[NKS+09] M. Narandzic, M. Käske, C. Schneider, G. Sommerkorn, A. Hong, W. A. Th. Kotterman, and R. S. Thomä. On a characterisation of large-scale channel parameters for distributed (multi-link) MIMO—the impact of power level differences. Technical Report TD-09-981, Braunschweig, Germany, February 2009.

[OCB+10] C. Oestges, N. Czink, B. Bandemer, P. Castiglione, F. Kaltenberger, and A. J. Paulraj. Experimental characterization and modelling of outdoor-to-indoor and indoor-to-indoor distributed channels. *IEEE Trans. Veh. Technol.*, 59(5):2253–2265, 2010. doi:10.1109/TVT.2010.2042475.

[PBK+10] A. Paier, L. Bernadó, J. Karedal, O. Klemp, and A. Kwoczek. Overview of vehicle-to-vehicle radio channel measurements for collision avoidance applications. In *Proc. VTC 2010 Spring—IEEE 71st Vehicular Technology Conf.*, Taipei, Taiwan, May 2010. [Also available as TD(09)928].

[PGR09] M. Park, P. Gopalakrishnan, and R. Roberts. Interference mitigation techniques in 60 GHz wireless networks. *IEEE Commun. Mag.*, 47(12):34–40, 2009.

[PHS+09a] J. Poutanen, K. Haneda, J. Salmi, V.-M. Kolmonen, F. Tufvesson, T. Hult, and P. Vainikainen. Development of measurement-based ray tracer for multi-link double directional propagation parameters. In *Proc. 3rd European Conf. Antennas and Propagation (EuCAP 2009)*, pages 2622–2626, Berlin, Germany, March 2009. [Also available as TD(09)771].

[PHS+09b] J. Poutanen, K. Haneda, J. Salmi, V.-M. Kolmonen, F. Tufvesson, and P. Vainikainen. Analysis of radio wave scattering processes for indoor MIMO channel models. In *Proc. PIMRC 2009—IEEE 20th Int. Symp. on Pers., Indoor and Mobile Radio Commun.*, Tokyo, Japan, September 2009. [Also available as TD(09)839].

[PJKK08] R. Piesiewicz, C. Jansen, M. Koch, and T. Kürner. Measurements and modeling of multiple reflections effect in building materials for indoor communications at THz frequencies. In *Proc. German Microwave Conference, GEMIC 2008)*, pages 3089–3092, Hamburg, Germany, March 2008. [Also available as TD(07)427].

[PKC+07] A. Paier, J. Karedal, N. Czink, H. Hofstetter, C. Dumard, T. Zemen, F. Tufvesson, C. F. Mecklenbräuker, and A. F. Molisch. First results from car-to-car and car-to-infrastructure radio channel measurements at 5.2 GHz. In *Proc. PIMRC 2007—IEEE 18th Int. Symp. on Pers., Indoor and Mobile Radio Commun.*, Athens, Greece, September 2007. [Also available as TD(07)303].

[PKH+08] R. Parviainen, P. Kyösti, Y.-T. Hsieh, P.-A. Ting, J.-S. Chiou, and M. Yang. Results of high speed train channel measurements. Technical Report TD(08)646, Lille, France, October 2008.

[PKZ+08] A. Paier, J. Karedal, T. Zemen, N. Czink, C. Dumard, F. Tufvesson, C. F. Mecklenbräuker, and A. F. Molisch. Description of vehicle-to-vehicle and vehicle-to-infrastructure radio channel measurements at 5.2 GHz. Technical Report TD(08)636, Lille, France, October 2008.

[PMB04] M. Pesavento, C. F. Mecklenbräuker, and J. F. Böhme. Multidimensional rank reduction estimator for parametric MIMO channel models. *EURASIP J. Appl. Signal Process.*, 2004(1):1354–1363, 2004.

[PQD+09] A. Panahandeh, F. Quitin, J. M. Dricot, F. Horlin, C. Oestges, and P. De Doncker. Cross-polar discrimination statistics for outdoor-to-indoor and indoor-to-indoor channels. Technical Report TD-09-815, Valencia, Spain, May 2009.

[PRK85] A. Paulraj, R. Roy, and T. Kailath. Estimation of signal parameters via rotational invariance techniques—ESPRIT. In *Proc. 19th Asilomar Conference on Circuits, Systems and Computers*, pages 83–89, Pacific Grove, CA, November 1985.

[Pro95] J. G. Proakis. *Digital Communications*, 2nd edition. McGraw-Hill, New York, USA, 1995.

[PSKK07] R. Piesiewicz, J. Schoebel, M. Koch, and T. Kürner. Propagation measurements and modeling for future indoor communication systems at THz frequencies. In *Proc. Wave Propagation in Communication, Microwave Systems and Navigation (WFMN 2007)*, Chemnitz, Germany, July 2007. [Also available as TD(07)367].

[PTA+10] A. Paier, R. Tresch, A. Alonso, D. Smely, P. Meckel, Y. Zhou, and N. Czink. Average downstream performance of measured IEEE 802.11p infrastructure-to-vehicle links. In *Proc. ICC 2010—IEEE Int. Conf. Commun.*, Cape Town, South Africa, May 2010. [Also available as TD(10)014].

[PZB+08] A. Paier, T. Zemen, L. Bernadó, G. Matz, J. Karedal, N. Czink, C. Dumard, F. Tufvesson, A. F. Molisch, and C. F. Mecklenbräuker. Non-WSSUS vehicular channel characterization in highway and urban scenarios at 5.2 GHz using the local scattering function. In *Proc. Int. Workshop Smart Antennas (WSA)*, pages 9–15, Darmstadt, Germany, 2008.

[QCOD07] F. Quitin, F. H. C. Oestges, and P. De Doncker. Cross-polarized MIMO channel measurements for indoor environments. Technical Report TD-07-388, Duisburg, Germany, September 2007.

[QOHD08a] F. Quitin, C. Oestges, F. Horlin, and P. De Doncker. Small-scale variations of cross-polar discrimination in polarized MIMO systems. Technical Report TD-08-603, Lille, France, October 2008.

[QOHD08b] F. Quitin, C. Oestges, F. Horlin, and P. De Doncker. Spatio-temporal characterization of polarized MIMO channels. Technical Report TD-08-602, Lille, France, October 2008.

[QOHDD10] F. Quitin, C. Oestges, F. Horlin, and P. De Doncker. A spatio-temporal channel model for modeling the diffuse multipath component in indoor environments. In *Proc. 4th European Conference on Antennas and Propagation (EuCAP 2010)*, Barcelona, Spain, April 2010. [Also available as TD(10)003].

[Ric05] A. Richter. *Estimation of radio channel parameters: models and algorithms*. PhD dissertation, Technischen Universität Ilmenau, Ilmenau, Germany, May 2005.

[RKVO08] O. Renaudin, V.-M. Kolmonen, P. Vainikainen, and C. Oestges. Wideband MIMO car-to-car radio channel measurements at 5.3 GHz. In *Proc. VTC 2008 Fall—IEEE 68th Vehicular Technology Conf.*, Calgary, Canada, September 2008. [Also available as TD(08)510].

[RKVO10] O. Renaudin, V.-M. Kolmonen, P. Vainikainen, and C. Oestges. Description of the August 2009 car-to-car radio channel measurement campaign. Technical Report TD(10)013, Athens, Greece, February 2010.

[RPZ09] L. Reichardt, J. Pontes, and T. Zwick. Performance improvement using multiple antenna systems for car-to-car communications in urban environment. Technical Report TD(09)966, Vienna, Austria, September 2009.

[RSK06] A. Richter, J. Salmi, and V. Koivunen. On distributed scattering in radio channels and its contribution to MIMO channel capacity. In *Proc. 1st European Conference on Antennas and Propagation (EuCAP2006)*, Nice, France, November 2006.

[RTR+08] A. Richter, F. Tufvesson, P. S. Rossi, K. Haneda, J. Koivunen, V.-M. Kolmonen, J. Salmi, P. Almers, P. Hammarberg, K. Pölönen, P. Suvikunnas, A. F. Molisch, O. Edfors, V. Koivunen, P. Vainikainen, and R. R. Müller. Wireless LANs with high throughput in interference-limited environments—project summary and outcomes. Technical Report TD-08-432, Wroclaw, Poland, February 2008.

[Sal09] J. Salmi. *Contributions to measeurement-based dynamic MIMO channel modeling and propagation parameter estimation*. PhD dissertation, Helsinki University of Technology, Dept. of Signal Processing and Acoustics, Espoo, Finland, August 2009. [Also available as TD(08)471].

[SCPF09] G. Steinböck, J.-M. Conrat, T. Pedersen, and B. H. Fleury. On initialization and search procedures for iterative high-resolution channel parameter estimators. Technical Report TD-09-956, Vienna, Austria, September 2009.

[SGL07] P. Stefanut, D. P. Gaillot, and M. Liénard. Parametric study of the performance of high-resolution estimation algorithms. Technical Report TD-09-763, Braunschweig, Germany, February 2007.

[SHK+07] J. Sachs, R. Herrmann, M. Kmec, M. Helbig, and K. Schilling. Recent advances and applications of m-sequence based ultra-wideband sensors. In *IEEE Intern. Conf. on Ultra-Wideband, ICUWB*, pages 50–55, September 2007. doi:10.1109/ICUWB.2007.4380914.

[SJK10] M. Schack, M. Jacob, and T. Kürner. Comparison of in-car UWB and 60 GHz channel measurements. In *Proc. The Fourth European Conference on Ant. and Prop. (EuCAP)*, pages 1–5, Barcelona, Spain, March 2010. [Also available as TD(10)11037].

[SKA+08] T. Santos, J. Karedal, P. Almers, F. Tufvesson, and A. Molisch. Scatterer detection by successive cancellation for UWB method and experimental verification. In *Proc. VTC 2008 Spring—IEEE 67th Vehicular Technology Conf.*, pages 445–449, Marina Bay, Singapore, May 2008. [Also available as TD(08)411].

[SKI+10a] K. Saito, K. Kitao, T. Imai, Y. Okano, and S. Miura. The DoA estimation method using EM/SAGE algorithm and extended MODE algorithm with array interpolation. Technical Report TD-10-12040, Bologna, Italy, November 2010.

[SKI+10b] K. Saito, K. Kitao, T. Imai, Y. Okano, and S. Miura. The modeling methods of time-correlated MIMO channels using the particle filter. Technical Report TD-10-11086, Aalborg, Denmark, June 2010.

[Smu02] P. F. M. Smulders. Exploiting the 60 GHz band for local wireless multimedia access: prospects and future directions. *IEEE Commun. Mag.*, 40(1):140–147, 2002.

[SOK+08] H. Singh, J. Oh, C. Kweon, X. Qin, H.-R. Shao, and C. Ngo. A 60 GHz wireless network for enabling uncompressed video communication. *IEEE Commun. Mag.*, 46(12):71–78, 2008.

[SPH+10] J. Salmi, J. Poutanen, K. Haneda, A. Richter, V.-M. Kolmonen, P. Vainikainen, and A. F. Molisch. Incorporating diffuse scattering in geometry-based stochastic channel models. In *Proc. 4th European Conference on Antennas and Propagation (EuCAP 2010)*, Barcelona, Spain, April 2010. [Also available as TD(10)047].

[SRE+06] J. Salmi, A. Richter, M. Enescu, P. Vainikainen, and V. Koivunen. Propagation parameter tracking using variable state dimension Kalman filter. In *Proc. VTC 2006 Spring—IEEE 63rd Vehicular Technology Conf.*, pages 2757–2761, Melbourne, Australia, May 2006.

[SRK09] J. Salmi, A. Richter, and V. Koivunen. Detection and tracking of MIMO propagation path parameters using state-space approach. *IEEE Trans. Signal Processing*, 57(4):1538–1550, 2009.

[SS90] P. Stoica and K. C. Sharman. Novel eigenanalysis method for direction estimation. *IEE Proc. Radar and Signal Processing*, 137(1):19–26, 1990.

[SSM10] J. Salmi, S. Sangodoyin, and A. F. Molisch. High resolution parameter estimation for ultra-wideband MIMO radar. In *The 44th Asilomar Conference on Signals, Systems, and Computers*, Pacific Grove, CA, November 2010. [Also available as TD(10)12042].

[SSN+09] C. Schneider, G. Sommerkorn, M. Narandzic, M. Käske, A. Hong, V. Algeier, W. A. T. Kotterman, and R. S. Thomä. Part I: Reference campaign—description and application. Technical Report TD-09-776, Braunschweig, Germany, February 2009.

[SV87] A. Saleh and R. Valenzuela. A statistical model for indoor multipath propagation. *IEEE J. Select. Areas Commun.*, 5(2):128–137, 1987.

[WAV] IEEE P802.11p/D4.0: Part 11: Wireless LAN Medium Access Control (MAC) and Physical Layer (PHY) Specifications: Amendment: Wireless Access in Vehicular Environments (WAVE), Draft 4.0, March 2008.

[WHR+10] S. Wyne, K. Haneda, S. Ranvier, F. Tufvesson, and A. Molisch. Beamforming effects on measured mm-wave channel characteristics. Technical Report TD-10-10023, Athens, Greece, February 2010.

[WWW+07] M. Webb, G. Watkins, C. Williams, T. Harrold, R. Feng, and M. Beach. Mobile multihop: Measurements vs. models. Technical Report TD-07-322, Duisburg, Germany, September 2007.

[Yin06] X. Yin. *High-resolution parameter estimation for MIMO channel sounding*. PhD dissertation, Department of Electronic Systems, Aalborg University, Aalborg, Denmark, 2006.

[YSH05] H. Yang, P. F. M. Smulders, and M. H. A. I. Herben. Indoor channel measurements and analysis in the frequency bands 2 GHz and 60 GHz. In *Proc. PIMRC 2005—IEEE 16th Int. Symp. on Pers., Indoor and Mobile Radio Commun.*, Dublin, Ireland, January 2005.

[YSK+08] X. Yin, G. Steinböck, G. E. Kirkelund, T. Pedersen, P. Blattnig, A. Jaquier, and B. H. Fleury. Tracking of time-variant radio propagation paths using particle filtering. In *IEEE International Conference on Communications (ICC 2008)*, pages 920–924, Beijing, China, May 2008. [Also available as TD(07)380].

[ZBN05] T. Zwick, T. J. Beukema, and H. Nam. Wideband channel sounder with measurements and model for the 60 GHz indoor radio channel. *IEEE Trans. Veh. Technol.*, 54(4):1266–1277, 2005.

[ZTE+10] M. Zhu, F. Tufvesson, G. Eriksson, S. Wyne, and A. F. Molisch. Parameterization of 300 MHz MIMO measurements in suburban environments for the COST 2100 MIMO channel model. Technical Report TD-10-11071, Aalborg, Denmark, June 2010.

http://www.springer.com/978-1-4471-2314-9

Pervasive Mobile and Ambient Wireless Communications
COST Action 2100
Verdone, R.; Zanella, A. (Eds.)
2012, XXXI, 677 p. 372 illus., 285 illus. in color.,
Hardcover
ISBN: 978-1-4471-2314-9